Atmospheric Monitoring System for VERITAS

Cloud Detection Using an Infrared Pyrometer and Atmospheric Attenuation Using Star Intensity

Kathleen Waller

Dated: May 4, 2006

Supervisory Committee:

David Kieda
Jordan Gerton
Kai Martens

Project Website: http://www.physics.utah.edu/~kieda/Atmosphere/

Abstract

This document discusses the design, analysis, and results of the atmospheric monitoring system for VERITAS. Much of this document also discusses complications with the atmospheric monitoring system and recommendations for future work. There are two major functions of this system, cloud detection and atmospheric attenuation measurements. Cloud coverage is detected with an infrared pyrometer and compared to the VERITAS trigger rate. Atmospheric attenuation is measured using star intensity detected with a CCD camera. The atmospheric monitoring system consists of an Astro Haven observatory dome, a Meade LX90 telescope with Autostar hand control, an ST-7 CCD camera with a UBVRI color filter wheel by Santa Barbara Instrument Group, and a KT15D infrared radiation pyrometer by Heitronics. All devices are interfaced using Labview 7.1 software.

Contents

List of Figures

List of Tables

List of Equations

I. Introduction

VERITAS is an array of telescopes under construction in Amado, Arizona[i]. Two of the four telescopes are currently operating at the base of Mt. Hopkins. This array is used to detect high energy ($E_\gamma > 10^{10} eV$) gamma rays entering the atmosphere. Determination of gamma ray energy depends on many factors including atmospheric conditions. Currently, the atmospheric conditions during an observation are simply given an A, B, C, or D grade determined visually by the observer at the beginning of the night. This grading procedure does not provide VERITAS with information that could be correlated with gamma ray observation data.

Figure 1: Artist Rendition of VERITAS[ii]

The atmospheric monitoring system will provide VERITAS a more accurate description of atmospheric conditions by detecting clouds with an infrared pyrometer and by measuring atmospheric attenuation.

Clouds are detected with an infrared pyrometer tracking the same region of sky over the same time span as VERITAS. This data may be correlated to VERITAS and may potentially be used to adjust the data gathered by VERITAS to account for clouds.

Atmospheric attenuation is the decrease in radiation due to the atmosphere. The atmospheric monitoring system is designed to measure attenuation by observing the change in intensity of a star over various atmospheric slant depths. Atmospheric attenuation is observed at ultraviolet, blue, visible, red, and infrared wavelengths by observing a star through a UBVRI filter wheel. This data may potentially by used to adjust data gathered by VERITAS to account for changes in altitude of a gamma ray source.

II. Background and Theory

A. VERITAS

VERITAS is an array of telescopes under construction in Southern Arizona. The objective of VERITAS is to detect gamma rays from outer space in an effort to probe some of the more interesting objects in our universe. Gamma radiation does not penetrate the Earth's atmosphere and is usually studied by detectors in satellites. However, this method is usually very costly and inefficient due to the relatively small detection area (~1 m^2).

Gamma rays can be detected through the Earth's atmosphere due to Cherenkov radiation. Each VERITAS telescope uses a large (144 m^2) segmented mirror and a 499 pixel camera employing photomultiplier tubes (PMTs) to detect Cherenkov radiation.

The sensitivity, or quantum efficiency, of the PMTs is shown in Figure 2. The peak of the quantum efficiency is at about 370 nm in the ultraviolet region of the electromagnetic spectrum.
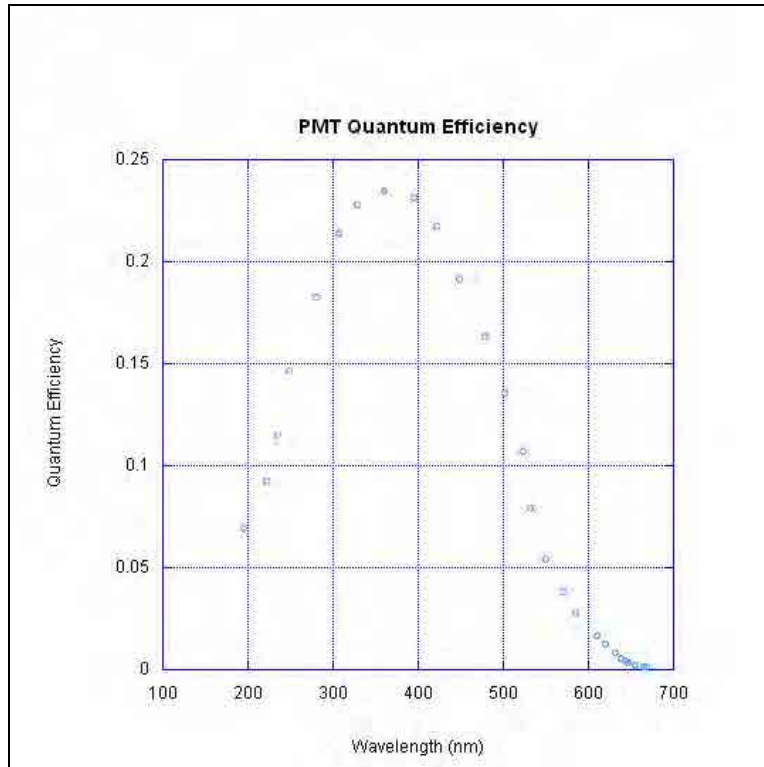
Figure 2: PMT Quantum Efficiency

The PMT's signals are compared to a variable threshold referred to as the trigger level. The number of PMT signals above the trigger level is referred to as the cosmic ray trigger rate. Variations in the trigger rate are not solely due to gamma ray source intensity fluctuations. Atmospheric attenuation and cloud coverage greatly influence the trigger rate. Variations in the trigger rate can be better understood through study of and comparison to atmospheric attenuation and cloud coverage.

Information about VERITAS is available at http://veritas.sao.arizona.edu/ .

B. Atmospheric Attenuation

The decrease in intensity of radiation through the atmosphere is known as attenuation. Attenuation is caused by scattering and absorption of photons off molecules and molecular elements in the atmosphere. Two major causes of attenuation are Rayleigh and Mie scattering.

1. Rayleigh Scattering

Rayleigh scattering refers to the scattering of photons off molecules. Rayleigh scattering can be considered to be elastic scattering since the energy of the scattered photons is not changed. Only

the direction of the photons is changed. Rayleigh scattering is polarization sensitive and more effective at wavelengths close to the blue and ultraviolet end of the spectrum. For example, it is Rayleigh scattering off the molecules in the atmosphere that gives us blue sky. In the atmosphere, Rayleigh scattering is primarily due to oxygen and nitrogen molecules.

The intensity of Rayleigh scattering is proportional to λ^{-4}. For example;

$$\lambda_{Blue} = 435 \text{ nm}, \qquad \lambda_{UV} = 365 \text{ nm},$$
$$\lambda_{Red} = 600 \text{ nm}, \qquad \lambda_{IR} = 780 \text{ nm},$$
$$(435/600)^{-4} = 3.6 \qquad (365/780)^{-4} = 20.9$$

(Wavelengths are defined by the peak transmissions of the CCD camera's color filter wheel.)

Therefore, blue light is scattered 3.6 times more than red light and ultraviolet light is scattered 20.9 times more than infrared light due to Rayleigh scattering.

2. Mie Scattering

Mie scattering refers to the scattering of photons off aerosols and particles that have a mean diameter 0.1 to 10 times the wavelengths of the incident photons. In the atmosphere, Mie scattering is primarily due to water vapor, smoke particles, and fine dust. Mie scattering off water vapor is responsible for the white and sometimes dark appearance of clouds.

The intensity of Mie scattering is proportional to λ^0 in the visible spectrum (depending on the particle's diameter). Therefore, Mie scattering is not strongly wavelength dependent in the visible spectrum.

3. Atmospheric Attenuation Measurements Using Star Intensity

In the absence of varying cloud conditions, star intensity may be used to calculate atmospheric attenuation due primarily to Rayleigh scattering and slightly due to Mie scattering.

The attenuation of star intensity by the atmosphere is calculated by recording the change in the intensity of a star versus change in altitude. The change in intensity is expressed as,

$$\frac{dI}{dT} = -\frac{I}{\tau},$$

Equation 1: Change in Intensity

where I is the intensity, T is the atmospheric slant depth, and τ is the atmospheric attenuation. The depth of the atmosphere is related to the altitude or angle above the horizon, θ, as,

$$T = \frac{T_0}{\sin(\theta)},$$

Equation 2: Thickness vs. Altitude

where T_0 is the depth of the atmosphere at zenith.
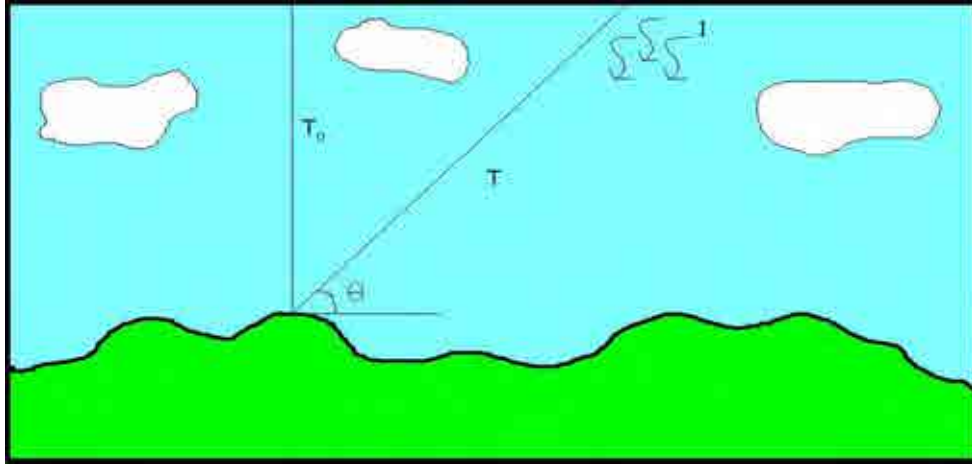
Figure 3: Atmospheric Slant Depth

After substituting Equation 2 into Equation 1 and integrating, the intensity of a star versus altitude is,

$$\ln(I) = \ln(I_0) - \frac{T_0}{\tau \times \sin(\theta)} .$$

Equation 3: Atmospheric Attenuation

A graph of $M0 = 1/sin(\theta)$ versus $y = ln(I)$ should be a straight line $(y = m1 + m2*M0)$ with a slope,

$$m2 = -\frac{T_0}{\tau} .$$

Equation 4: Atmospheric Attenuation Slope

The slope gives the ratio of atmospheric attenuation to the depth of the atmosphere at zenith. Since the slope does not have units, the units of atmospheric attenuation are equal to the units used to define the depth of the atmosphere at zenith.

In order to calculate atmospheric attenuation, we need to know the depth of the atmosphere at zenith. Due to the structure of the atmosphere, this value is not well defined. The following sources give atmospheric depth values with respect to sea level:

Earth Science. USA: Prentice Hall, 1987 pg 309	1000 km
World Book Encyclopedia. World Book, 1998 pg 19	1600 km
Focus on Earth Science. USA: Merrill, 1979 pg 339	700 km

The average and most often used value of depth is 1000 km. This value is attributed to the ability to detect any particles constituting atmosphere. Assuming the elevation at the observation site is 1.275 km, the depth of atmosphere at zenith at the observation site is,

$$T_0 = 998.725 \, \text{km}.$$

8

Due to the very low density of particles at 1000 km, very little radiation is attenuated at 1000 km. This value may predict the presence of particles constituting atmosphere but is a very extreme value for the sake of atmospheric attenuation measurements.

Another method of defining atmospheric depth is related to the density of particles versus elevation. A graph of density versus elevation is provided at http://www.pdas.com/atmthick.htm[iii]. According to this site, 99% of the total mass of the atmosphere is contained within 31 km from sea level. Therefore, the depth of the atmosphere at zenith at the observation site is,

$$T_0 = 29.725 \, \text{km}.$$

One more method of defining depth of the atmosphere is by using pressure. Atmospheric pressure is the mass above a certain elevation per unit area. For simulations, VERITAS uses,

$$T_0 = 815.5 \, \text{g/cm}^2.$$

to describe the pressure of the atmosphere at the observation site. This value follows the convention of VERITAS. As a result, the atmospheric attenuation is reported in units of g/cm^2. The atmospheric attenuation length is found by dividing the pressure by the density of the atmosphere at sea level, $\rho_{\text{sea level}}$,

$$\rho_{\text{sea level}} = 1.2 \times 10^3 \, \text{g/cm}^3.$$

For the purpose of this document, the atmospheric attenuation is reported using all three definitions of depth of the atmosphere at zenith at the observation site. Due to their arbitrary nature and lack of error values in these definitions, the real values of importance are the slopes derived from the graphs of $M0 = 1/sin(\theta)$ versus $y = ln(I)$. The final results for atmospheric attenuation lengths are calculated using atmospheric pressure and density. These results are comparable to expected attenuation lengths due to Rayleigh scattering.

Previous and similar work in measuring atmospheric attenuation is being done by various groups. Most relevant to this document is work done by a former member of VERITAS, Gary Walker. The base site location mentioned in his work is the same observation site used for my data collection. Although his work is equivalent in equipment and location, comparisons are difficult to make due to a lack of specific information pertaining to data collection. His work does offer a unique method of measuring attenuation length by collecting data at two significantly distinct elevations. His method avoids the problem of defining the depth of the atmosphere at zenith by knowing the difference in elevations at two sites. The difference in slopes of $M0 = 1/sin(\theta)$ versus $y = ln(I)$ and difference in elevations are used to calculate atmospheric attenuation length, τ,[iv]

$$\tau = \frac{\Delta Elevation}{\Delta Slope}$$

Equation 5: Atmospheric Attenuation Using ΔElevation

.

C. Clouds

The above discussion of atmospheric attenuation omitted the effects of clouds. Clouds attenuate radiation primarily by Mie scattering. The density of clouds is usually not consistent over the sky and interferes with the ability to measure high energy gamma rays and atmospheric attenuation. Therefore, it is necessary to understand and detect clouds.

Most cloud droplets are so large (>20 µm) they scatter all visible wavelengths more or less equally. Because all wavelengths are scattered, clouds appear to be white. When clouds become very dense, less of the incoming solar radiation makes it through the clouds, giving them a darker appearance.

Other constituents, such as large aerosols, volcanic ash, and smog, scatter light independent of wavelength. Most of these particles are consistent over the sky and only result in a shift in atmospheric attenuation.

Clouds are composed of water, a very strong absorber of electromagnetic radiation in the far-infrared region. The IR pyrometer used in the atmospheric monitoring system has a spectral response of 8…14 µm, placing it on the border between far-infrared and mid-infrared. The IR pyrometer reports electromagnetic radiation on a temperature scale. The temperature response of the IR pyrometer is $\geq$ -50 ^{0}C. This temperature response works well for distinguishing clouds against clear sky in Arizona year round. Clouds are detected by observing an increase in the IR pyrometer temperature reading compared to clear sky. Unfortunately there is not a means of determining an absolute scale of cloud coverage due to the overall change in humidity and ambient temperature over the course of the seasons.

The IR pyrometer is mounted in parallel with a CCD camera used to collect star light for atmospheric attenuation measurements. Using this configuration, cloud coverage is determined at the same time and location of the star being used to determine atmospheric attenuation. Three examples of cloud coverage are shown in Figure 15, Figure 16, and Figure 17 of this document. By measuring cloud coverage with the IR pyrometer, I am able to determine whether or not the sky is clear enough to calculate atmospheric attenuation.

The IR pyrometer is also used to compare cloud coverage to the VERITAS trigger rate to determine if there exists a correlation. As long as the Cherenkov radiation shower is produced above the clouds, the IR pyrometer and trigger rate should be comparable. Future work may involve testing the ability to measure cloud height with the IR pyrometer. Initial tests would include measuring a terrestrial object at constant temperature at varying distances to show IR temperature varies with distance.

At the time of writing this document, VERITAS does not measure cloud coverage with an IR pyrometer. Currently, cloud coverage and atmospheric conditions during an observation are simply given an A, B, C, or D grade, determined visually by the observer at the beginning of the night. Various resources are available to assist in determining atmospheric conditions including wind and humidity detectors, and an all sky camera located above the observation site at the Multi-Mirrored Telescope[v]. Currently, none of these indicators are directly compared to VERITAS data. The IR pyrometer can provide cloud coverage information for direct comparison to VERITAS. Continuing work for VERITAS will likely include installing one IR pyrometer on each VERITAS telescope, viewing the same region of sky.

HESS, a similar telescope array in Namibia, has already install IR pyrometers on each of its telescopes. An article submitted by HESS at the 28th International Cosmic Ray Conference

demonstrates a correlation between IR pyrometer temperatures and telescope trigger rates. This article serves as further support for installing one IR pyrometer on each VERITAS telescope.[vi]

III.Design

Figure 4: Atmospheric Monitoring System

The atmospheric monitoring system consists of an Astro Haven observatory dome, a Meade LX90 telescope mount with Autostar hand control, an ST-7 CCD camera with a UBVRI filter wheel by Santa Barbara Instrument Group, and a KT15D infrared radiation pyrometer by Heitronics. The observatory dome and all devices sit above a trailer. Inside the trailer is a computer workstation where all devices are interfaced using Labview 7.1 software. Much of the collected data is processed using Labview 7.1 and NI Vision software. Collected and processed data is written to ASCII text format files. These files are further analyzed using KaleidaGraph 4.0 software.
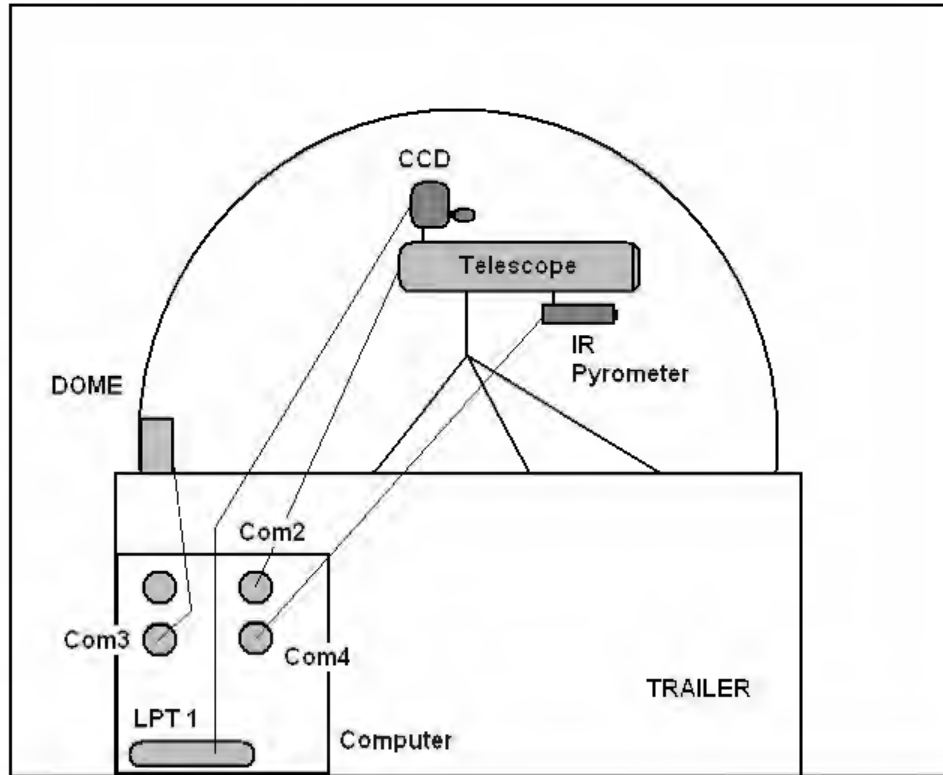
Figure 5: Atmospheric Monitoring System Diagram

A. Astro Haven Observatory Dome

The observatory dome is opened and closed by the computer through a serial connection. The observatory dome can also be opened and closed from inside the dome at the control box.

Figure 6: Observatory Dome Control Box and South Side Motor

The computer sends and receives ASCII text string commands to and from the control box inside the dome. These commands are easily implemented using HyperTerminal. A simple Labview virtual instrument (VI) is also set up to allow a user to open and close the dome with a virtual switch and without knowledge of the string commands. This VI and other information related to the observatory dome are available at http://www.physics.utah.edu/~kwaller/Atmosphere/Dome/ .

During the design and analysis of the atmospheric monitoring system, the dome would often time not close when instructed. Through trial and error, it was deduced that this problem most likely was caused by failure of one of the magnetic sensors. The observatory dome is equipped with four magnetic sensors, two for either side, that indicate when the dome is fully opened or closed. On random occasions a sensor would be stuck in the wrong position resulting in a response from the control box that the dome is always closed. This problem is usually resolved by tapping on the outside of the dome behind the magnetic sensor. One should replace these sensors if this problem continues to occur.

The current configuration consists of Astro Haven Observatory Dome #30307 connected to the Com3 serial port. The related VI will not work if the observatory dome is connected to any other port on the computer.

The string commands and responses to communicate with the observatory dome are:

String Commands:	String Responses:
Open South = a	South Opening = a
	South Open = x
Close South = A	South Closing =A
	South Closed = X
Open North = b	North Opening = b
	North Open = y
Close North = B	North Closing = B
	North Closed = Y

B. Heitronics KT15.82D Infrared Radiation Pyrometer

The infrared (IR) radiation pyrometer is attached to the underside of a Meade LX90 telescope. The IR pyrometer is controlled by the computer through a serial connection.

The current configuration consists of a KT15-82D Type A. IR pyrometer connected to the Com4 serial port. Related VI's will not work if the IR pyrometer is connected to any other port on the computer. The IR pyrometer is disconnected at the pyrometer when not in use to prevent any damage from electric shock.

Figure 7: IR Pyrometer

The computer sends and receives ASCII text string commands to and from the IR pyrometer. These commands and responses are described in the IR Pyrometer Operating Instructions[vii]. These commands are easily tested using HyperTerminal. Individual Labview VI's were built corresponding to each of the commands described in the operating manual. Figure 8 is an example VI used to query the serial number of the IR pyrometer. These VI's also serve the purpose of formatting many of the string responses into numeric indicators or string formats appropriate for data logging. VI's and other information related to the IR pyrometer are available at http://www.physics.utah.edu/~kwaller/Atmosphere/IRPyrometer/ .
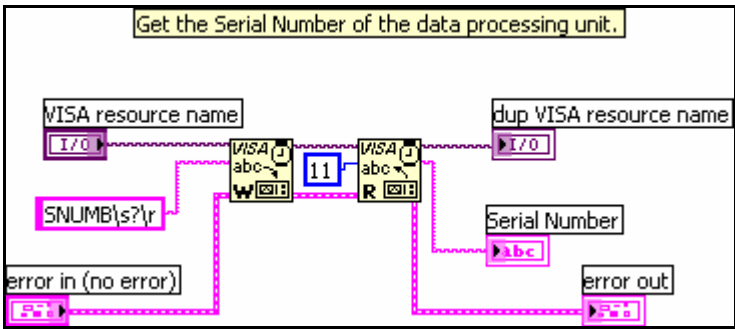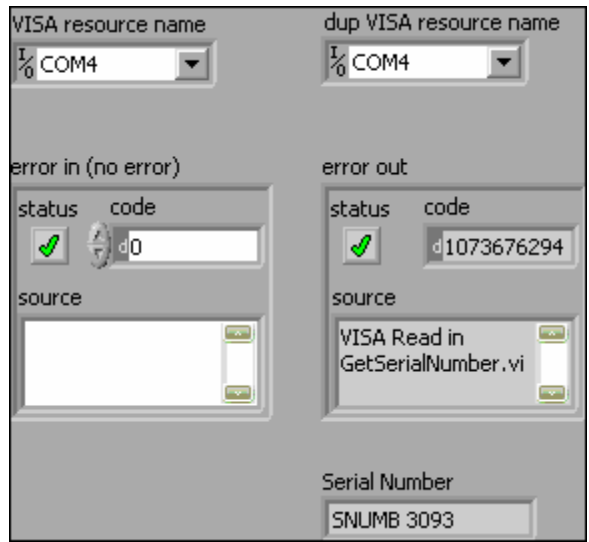
Figure 8: Example IR Pyrometer VI

The KT15D IR Pyrometer has a spectral response of 8…14 μm and a temperature response ≥ -50 $^{\circ}$C. The field of view of the IR pyrometer is 2.9 $^{\circ}$. The following response times are available for the IR pyrometer: 0.05, 0.1, 0.3, 1, 3, and 10 sec. Longer response times reduces have lower temperature resolution. Using the KT15.82D Type A. IR pyrometer at a 1 second response time and 1.000 emissivity, the temperature resolution is 0.2 $^{\circ}$C for temperature readings of 20…-25 $^{\circ}$C. For the atmospheric monitoring system, this resolution is more than sufficient. For future work, it may be possible to reduce the response time for faster data collection while maintaining sufficient temperature resolution. [viii]

The issue of properly aligning the IR pyrometer to the Meade LX90 telescope pointing axis was not addressed in the design of the atmospheric monitoring system. For the purpose of this document, it is assumed that the IR pyrometer is within 2.9 $^{\circ}$ of the Meade LX90 optical axis and therefore any error in the alignment may be ignored. Future work may include designing an apparatus for properly aligning the IR pyrometer. This would most likely include mounting a point source detectable to both the Meade LX90 optics and the IR pyrometer in the vicinity of the monitoring system.

The optics of the IR pyrometer is covered when it is not in use to protect the pyrometer from damage from the sun. It is important to never point the IR pyrometer directly at the sun to avoid permanent damage.

C. SBIG ST-7 CCD Camera

An ST-7 CCD camera by Santa Barbara Instrument Group is used to detect star light for atmospheric attenuation measurements. The CCD is mounted "piggy-back" to the Meade LX90 telescope. The CCD camera does not use the optics of the telescope. The optics of the telescope is only used to align the CCD camera to the telescope.

The CCD camera is connected to the LPT1 parallel port. Related VI's will not work if the CCD camera is connected to any other port on the computer.

The CCD camera is adapted with a CFW-8A UBVRI color filter wheel by Santa Barbara Instrument Group. The optics of the camera is a BK7 F4 achromatic doublet lens, designed and built by Gary Walker[ix].

VI's and other information related to the CCD Camera are available at
http://www.physics.utah.edu/~kwaller/Atmosphere/CCDCamera/ .

1. Camera

The CCD camera is a dual imaging camera; it has both a tracking and imaging CCD chip. The tracking chip is not used in this monitoring system.

At high resolution (1 X 1 pixel), the imaging chip has the following specifications:

- CCD image width: 765 pixels
- CCD image height: 510 pixels
- pixel width: 9.00 μm
- pixel height: 9.00 μm
- gain: 2.30 (e-/ADU)*
                          *Electrons per Analog to Digital Units

Interfacing with the CCD camera was one of the more difficult tasks in designing the atmospheric monitoring system. Communication does not flow directly from the Labview software to the CCD camera. The Labview software is connected to a dynamic link library (DLL), sbigudrv.dll[x], which then communicates with the CCD camera. Santa Barbara Instrument Group provides documentation to interface with the DLL[xi]. The following is an example, taken from that documentation, of how to call the DLL in order to start a CCD exposure.

> The software interface to the Universal Driver Library is through a single external function that takes a short integer **Command** and pointers to two structs: command **Parameter** and command **Results**. The driver acts upon the **Command** and **Parameters** struct and fills in the **Results** struct. The memory allocation for these structs is the responsibility of the calling program.
>
> The C prototype for the function is shown in the SBIGUDRV.H file and takes the form:
>
> short **SBIGUnivDrvCommand** (short **Command**, void *****Parameters**, void *****Results**)

where **Command** is the command to be executed and **Parameters** and **Results** are pointers to the structs.

…

Some commands don't require **Parameters** structs and some don't require **Results** structs. In those cases you should pass a NULL pointer to the driver.

…

The Start Exposure command is used to initiate an exposure. The application specifies the exposure time, etc. and then monitors the exposure's progress with the Query Command Status command discussed below.

> *Parameters Struct:*
>
> > struct **StartExposureParams {**
> > > enum **ccd** - the CCD to use in the exposure
> > > > 0 = Imaging CCD
> > > > 1 = Tracking CCD
> > > > 2 = External Tracking CCD in ST-L
> > >
> > > ulong **exposureTime** - integration time in
> > > > hundredths of a second in the least significant 24
> > > > bits. The most significant 8 bits are bit-flags that
> > > > modify the exposure as described below.
> > >
> > > enum **abgState** - antiblooming gate state during
> > > > integration
> > > > 0 = Low during integration (ABG shut off)
> > > > 1 = Clocked at low rate
> > > > 2 = Clocked at medium rate
> > > > 3 = Clocked at high rate
> > >
> > > enum **openShutter**
> > > > 0=Leave Shutter alone
> > > > 1=Open Shutter for Exposure and Close for
> > > > Readout,
> > > > 2=Close Shutter for Exposure and Readout
> >
> > **}**

The sbigudrv.dll is a 32 bit Windows DLL. It is built with the "stdcall" calling convention, which means it can be called from Visual C++ or Visual Basic. Calling the DLL with Labview is a bit more complicated. National Instruments offers a help document on communicating to a DLL with Labview, *Using External Code in Labview[xii]*.

Figure 9 is an example VI used to start an exposure by communicating with the DLL file.
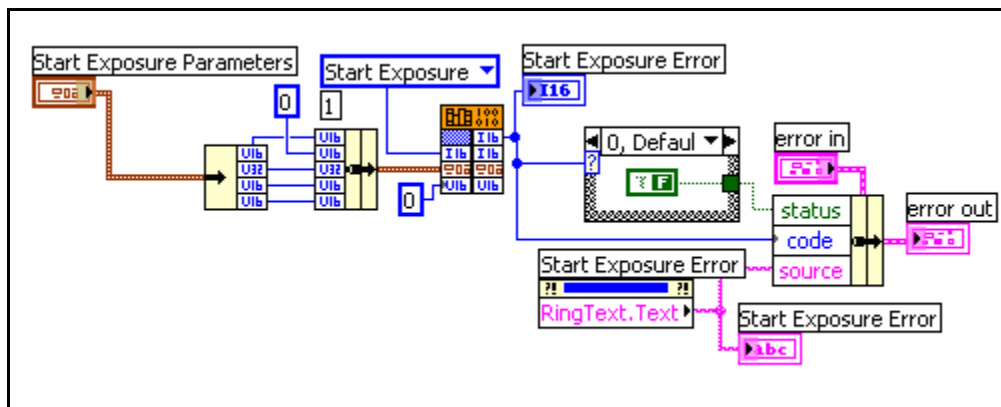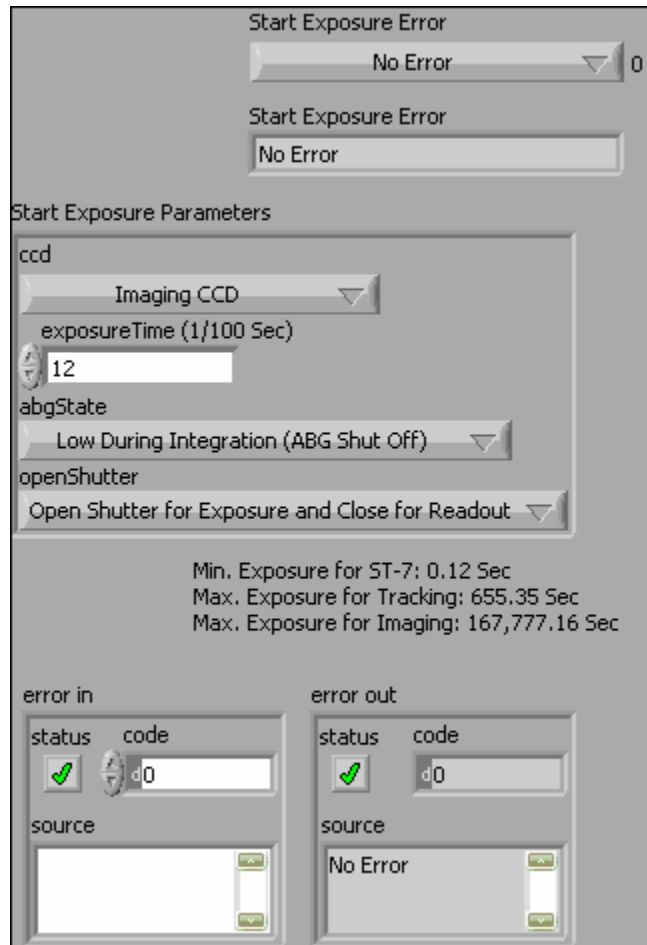
Figure 9: Example CCD Camera VI

The three inputs of the "Call Library Node" are **Command**, **Parameters**, and **Results**. The designations of the enumerated input **Command** can be found in sbigudrv.h[xiii]. The input **Results** is passed a NULL, 0, because there is no **Results** structure associated with the **Start Exposure** command.

The **Parameters** input is simulated with a cluster. Note the ushort 0 padding after the enum **ccd**. This padding is necessary to force the Labview cluster to line up with the DLL structure. Structures in Labview do not simply line up with clusters in C code due to a difference in pragma packing between the two languages. Further discussion on this topic is available through National Instruments, *Why Do My Clusters in Labview Not Line Up With My Structures in C?*[xiv].

2. CFW-8A Filter Wheel[xv]

The CCD camera is equipped with a CFW-8A color filter wheel by Santa Barbara Instrument Group. The filter wheel is equipped with ultraviolet, blue, visible, red, and infrared filters. Table 1, Figure 10, and Figure 11 show the position of each filter and the transmission band of each filter. Manuals and detailed transmission graphs for each filter are available at http://www.physics.utah.edu/~kwaller/Atmosphere/CCDCamera/CFWFilter/ . **Calibration**, **Initialize**, and **Power On** all set the filter wheel to the red filter.
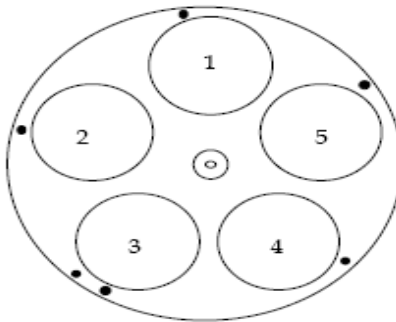
Figure 10: Top View of the CFW Filter Wheel

Table 1: Filter Transmission Band Centers and Positions

Filter	Band Center (nm)	Wheel Position
Ultraviolet	365	4
Blue	435	3
Visible	525	2
Red	600	1
Infrared	780	5
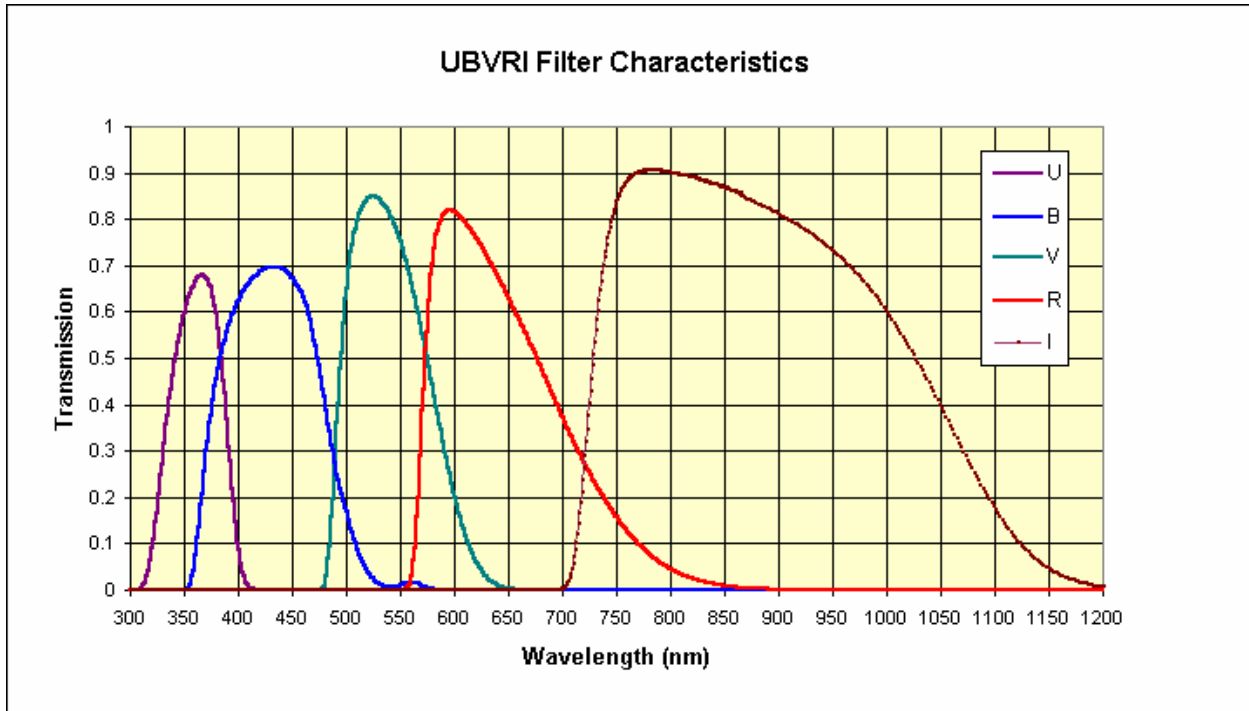
Figure 11: Filter Wheel Transmission Bands

The CFW-8A filter wheel is interfaced by the sbigudrv.dll through the CCD camera.

3. CCD Camera Lens

The optics of the CCD camera is a 25-mm achromatic doublet lens used to image onto the CCD chip. The focal length of the lens is 100 mm with a 3^0 field of view.

A doublet is a lens made of two materials. This helps to reduce aberration in the optics by using one material that cancels out the aberrations of the other.

The doublet is made of BK7 (Borosilicate Crown) and F4 (Dense Flint) glass. The transmission ranges of both materials extend well into the infrared. BK7 cuts off below 340 nm in the ultraviolet and F4 cuts off below 360 nm in the ultraviolet. Therefore, the cutoff wavelength of the lens is above the cutoff of the ultraviolet filter in the CFW-8A filter wheel and above the cutoff of the VERITAS PMTs (see Figure 2 and Figure 11). This lens works well for observing star light across a wide spectrum but does not work well for viewing star light in the ultraviolet. Future work may involve measuring atmospheric attenuation in the ultraviolet part of the spectrum with a different lens.

The lens is covered when not used to prevent dust build-up and damage to the CCD camera from the sun.

D. Meade LX90 Telescope w/ Autostar

Figure 12: Autostar Hand Control

The IR pyrometer and CCD camera are aligned to sources using a Meade 8" LX90 Schmidt-Cassegrain telescope with Autostar Hand Controller. The telescope is controlled by the Autostar which is connected to the computer through an adapted serial connection.

The current configuration consists of the Autostar connected to the Com2 serial port. Related VI's will not work if the Autostar is connected to any other port on the computer. A helpful document for connecting the Autostar Hand Control to the computer is available at http://www.weasner.com/etx/fun/etx_star_party_2002/etx90ec-talk.zip [xvi].

VI's and other information related to the Meade LX90 telescope are available at http://www.physics.utah.edu/~kwaller/Atmosphere/Mount/ .

The computer sends and receives ASCII text string commands to and from the Autostar. These commands and responses are outlined in the *Meade Telescope Serial Command Protocol*[xvii]. Individual Labview VI's were built corresponding to each of the commands described in the Protocol and available for Autostar. These VI's also serve the purpose of formatting many of the string responses into numeric indicators or string formats appropriate for data logging. Figure 13 is an example VI used to query the altitude of the telescope.
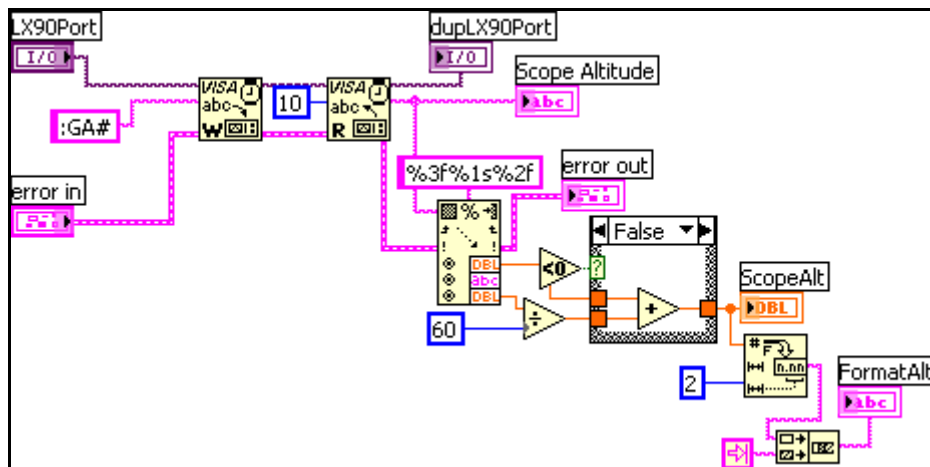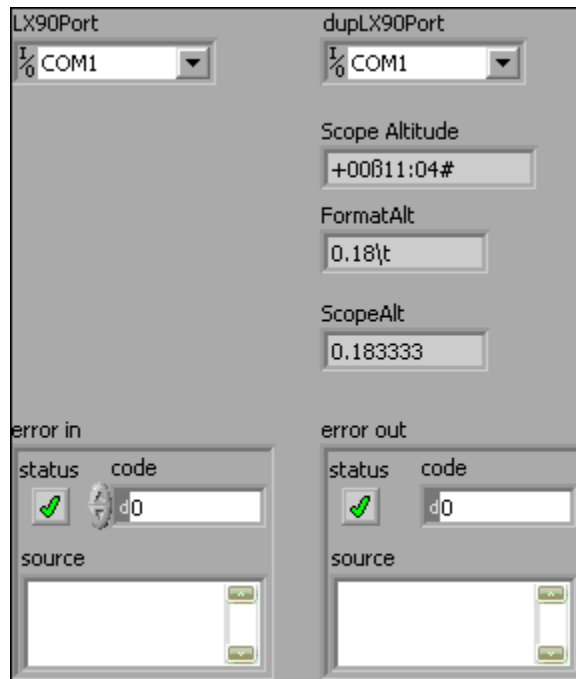
Figure 13: Example LX90 Telescope VI

While designing the atmospheric monitoring system, I found that many of the commands in the *Telescope Serial Command Protocol* did not work as expected. Therefore, controlling the movement of the telescope was extremely difficult to do through the computer. Aligning the telescope is impossible to do through the computer using the commands available in the protocol. For the atmospheric monitoring system, only commands which query and set date, time, and location information are used. Alignment of the telescope must be done manually using the Autostar hand control as outlined in the Meade LX90 instruction manual[xviii]. I choose to use the "Easy, Two Star" align option when operating the telescope.

By using the "park telescope" command outlined in the operating manual and available as a VI, the telescope is brought back to 0^0 azimuth and 0^0 altitude before turning off the telescope. This makes aligning the telescope much easier next time it is used.

Other topics of importance for operating the Meade telescope include; preventing cord wrap, training the drives, and configuring to computer date and time.

Preventing cord wrap is very important when using the atmospheric monitoring system. Considering the equipment mounted on the Meade telescope and the cords for operating the telescope, it is easily possible to damage the equipment by letting the telescope move too far in any direction. One helpful solution is to set the "Cord Wrap" option on the Autostar to "On". This prevents the telescope from moving more than 360 ^{0} in azimuth in either direction. In the early stages of design, a USB camera was used to monitor the telescope while moving. The camera could only be used during daylight hours to practice moving the mount remotely. If future work involves moving the telescope remotely at night, the USB monitoring camera may need to be employed with a red LED backlight for illumination.

The Meade LX90 instruction manual recommends training the drives twice a year or any time equipment is added to or removed from the telescope. This helps to improve the tracking capability of the telescope. The telescope movement is controlled by two drives, one for azimuth and one for altitude. The process of training the drives is done during daylight hours using a terrestrial object. The process of training the drives in outlined in the Meade LX90 instruction manual.

When the Meade telescope is turned on, it prompts for the date and time. To reduce error in collected data it is best to set the telescope to the computer date and time. In order to do this the user must first skip through the date, time, and Daylight Savings prompts on the Autostar hand control (Arizona does not recognize Daylight Savings). The date and time are set to the computer date and time using the "Set Hand Box Date" and "Set Local Time" commands implemented as VI's. Figure 14 shows how Labview gets the computer local time and sets the telescope time.

Figure 14: Set Autostar to Local Time VI

By setting the telescope date and time to the computer date and time, all data related to position of objects in the sky are as accurate as the time stamp of the computer.

IV. Results

## *A. Cloud Detection Using an Infrared Pyrometer*

Cloud coverage was monitored using the IR pyrometer. Cloud coverage data was compared to star intensity measured by the CCD camera, and cosmic ray trigger rates measured by VERITAS. Correlation was measured between the IR pyrometer and ultraviolet star intensity on March 5th and is shown in Appendix V. During Spring 2006, joint observations between VERITAS, the IR pyrometer, and the CCD camera were collected over 23 nights.

The KT15-82D Type A. IR pyrometer was mounted to the underside of the Meade telescope optics. The IR pyrometer was visually aligned with the mount's azimuth axis. The IR pyrometer was connected to the Com4 serial port of the control computer.

The IR pyrometer was set to 1 second response time and 1.000 emissivity. The temperature resolution of the IR pyrometer was 0.2 ^{o}C for temperature readings of 20…-25 ^{o}C.

Figure 15, Figure 16, and Figure 17 show the results for the IR pyrometer for three separate nights. The error bars are not shown due to the relative size with respect to the y-axis. The x-axis is the altitude coordinate given by the Meade telescope. The error in the altitude is considered zero since the object (Sirius) is aligned in the center of the telescope optics and the time of the telescope is set to the computer time.

Figure 15 is the result of tracking Sirius from 42 ^{0} to 5 ^{0} altitude on February 4th. The scatter in the IR temperature represents a cloudy night. The overall slope to the graph is due to the increase in thickness of the atmosphere when Sirius is lower in the horizon. Atmospheric attenuation data was also collected February 4th. The optical intensity of the star was strongly affected by the changing clouds and therefore was not useful for data analysis.
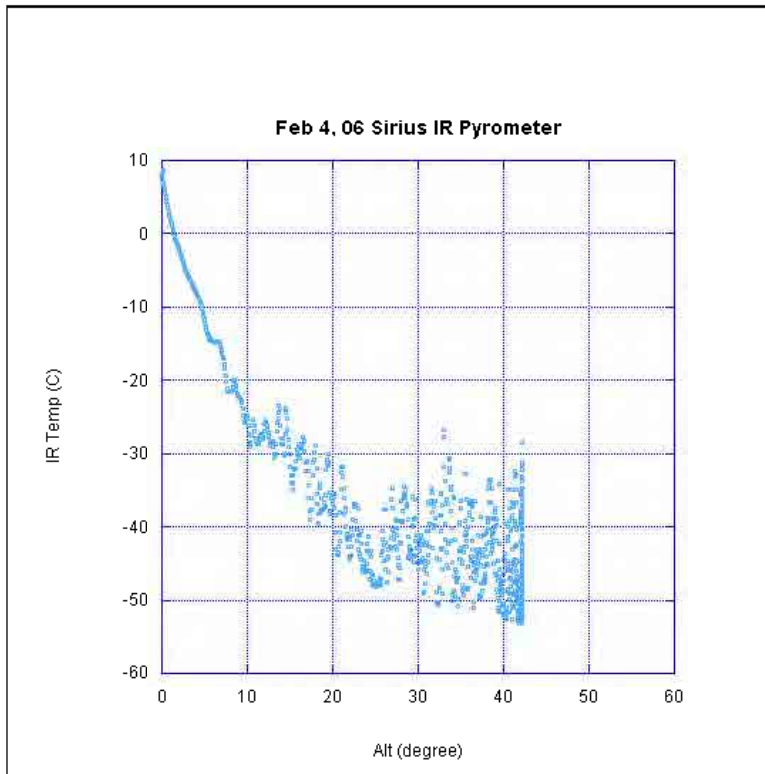
Figure 15: Cloudy

Figure 16 is the result of tracking Sirius from 41 ^{0} to 1 ^{0} altitude on March 1st. The sky was very cloudy for the first half of the night, and very clear when Sirius was below 25 ^{0} altitude. Atmospheric attenuation data was also collected on March 1st. Each point in this graph corresponds to an exposure taken by the CCD camera for atmospheric attenuation data. By plotting *sin(1/alt)* versus *ln(IR Temp)* Figure 16 fits well to a straight line for altitude > 25 ^{0}. Points not fitting the line can be removed. CCD exposures corresponding to IR temperatures not fitting the straight line were omitted.
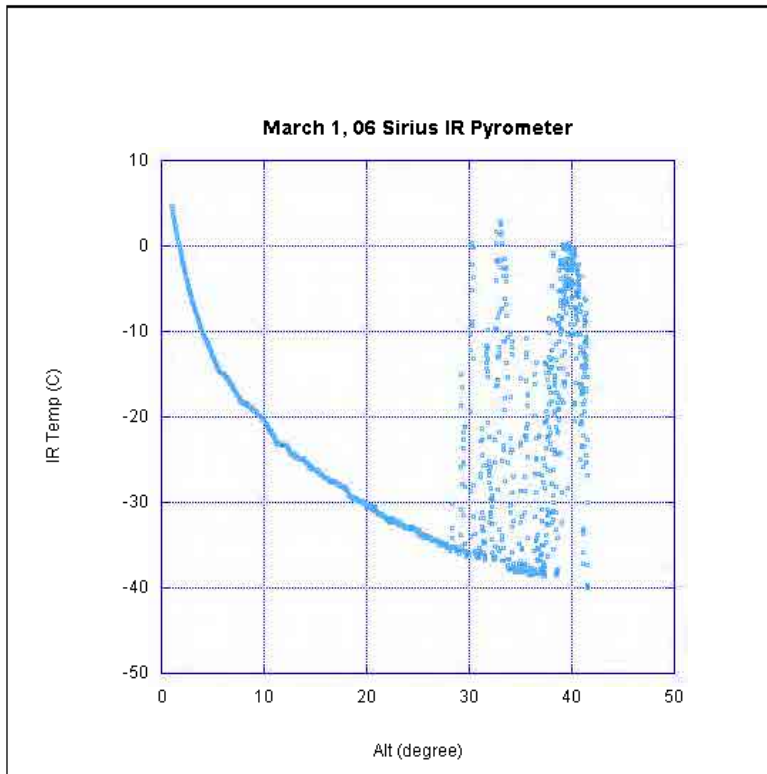
Figure 16: Partly Cloudy

Figure 17 is the result of tracking Sirius from 42 ^{0} to 3 ^{0} altitude on February 24th. The sky was visually very clear.
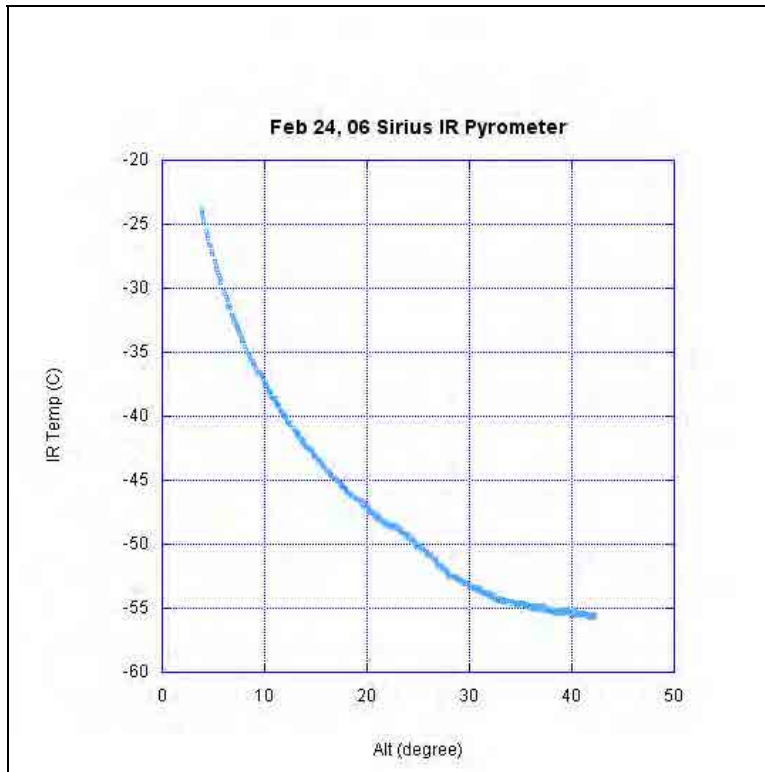
Figure 17: No Clouds

Similar IR pyrometer data was collected for all nights while collecting atmospheric attenuation data. The IR pyrometer data was used to asses whether to use that night's CCD camera data for atmospheric attenuation analysis. IR temperature graphs of nights used for atmospheric attenuation analysis are shown in Appendix I, Appendix II, Appendix III, and Appendix IV.

1. Clouds versus VERITAS Trigger Rate

Cloud coverage was compared to the VERITAS trigger rate on two separate nights, March 1st and March 5th. Both nights were particularly cloudy. The data was collected by pointing both the atmospheric monitoring Meade telescope and the VERITAS telescopes at the same sky location. Data was simultaneously collected by both VERITAS and the IR pyrometer. The data was compared using Pearson's Correlation Coefficient.

Pearson's Correlation Coefficient, R, is a quantity that defines the quality of a least squares fitting to a set of data[xix]. In the case of a linear least squares fit, Pearson's Correlation Coefficient, R, is defined as,

$$R = \frac{n \sum xy - \sum x \sum y}{\sqrt{[n \sum x^2 - (\sum x)^2][n \sum y^2 - (\sum y)^2]}},$$

Equation 6: Pearson's Correlation Coefficient

where x and y make up the data set and n is the number of data points. A data set that is highly correlated will have an R value close to 1 or -1. R close to or equal to 0 indicates no correlation. If the VERITAS trigger rate is correlated to the IR pyrometer, a graph of x = *IR Temp* and y =

Trigger Rate should have an *R* value close to -1. The slope should be negative to since the IR pyrometer represents clouds with low temperatures and clear sky with high temperature. The actual data was plotted as *x* = *-IR Temp* and *y* = *Trigger Rate* to show a positive correlation.

a) March 1, 2006 T2 Trigger Rate vs. IR Pyrometer

March 1st was used to compare the VERITAS cosmic ray trigger rate and the IR pyrometer temperature. Only VERITAS telescope number two (T2) was used to collect the trigger data. T2 and the atmospheric monitoring Meade telescope tracked Regulus. Regulus was chosen because it is a very bright star and could be seen through most of the clouds. The IR pyrometer was set to a 1 second response time and the T2 trigger rate data was stored in 1 second bins. The UTC time was logged with both data sets such that the data could be compared. Due to the dead time of the IR pyrometer VI's, every few seconds a data point was omitted from the IR pyrometer data. These points are masked or ignored when calculating the correlation, *R*.

The following graphs show the results of. Data related to Figure 18, Figure 19, Figure 20, Figure 21, and Figure 22 are available at http://www.physics.utah.edu/~kwaller/Atmosphere/ under "Clouds vs. T2 Trigger Rate" data.

Figure 18 shows UTC time versus –IR temperature. The temperature resolution is 0.2 ^{0}C. The IR temperature error bars are not shown due to their relative size to the y-axis. The negative temperature was used such that lower y-axis values will indicate clouds.
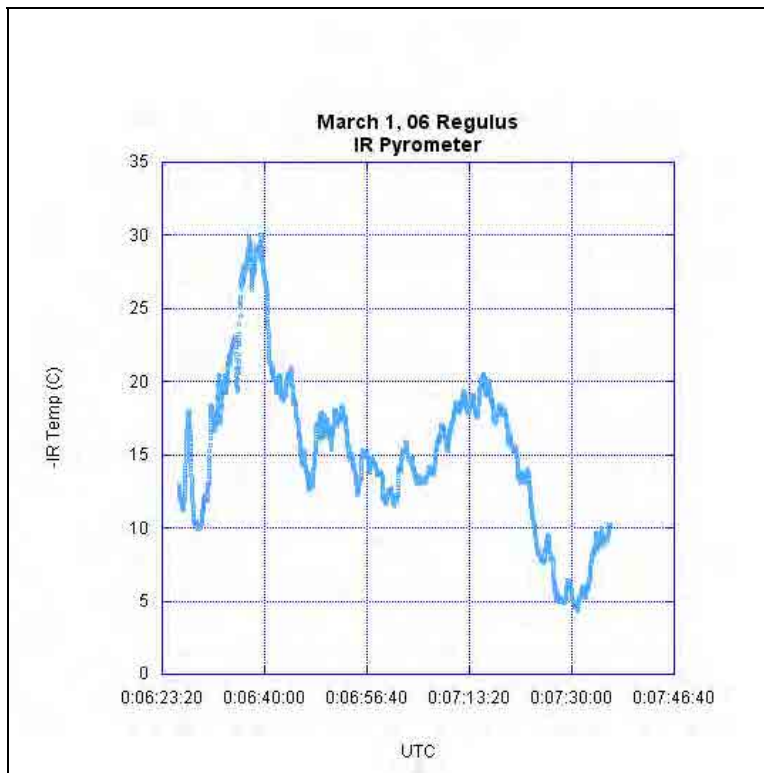

Figure 18: March 1, 06 IR Pyrometer

Figure 19 shows raw data of T2 cosmic ray trigger rate versus UTC time. The error in the T2 trigger rate is equal to the square root of the trigger rate. This error is approximately equal to the spread in the data points in the y-axis. The correlation between the T2 trigger rate and the IR pyrometer is not obvious. A boxcar average was applied to the trigger rate data to reduce the spread in the points and show a better visual correlation to the IR pyrometer.
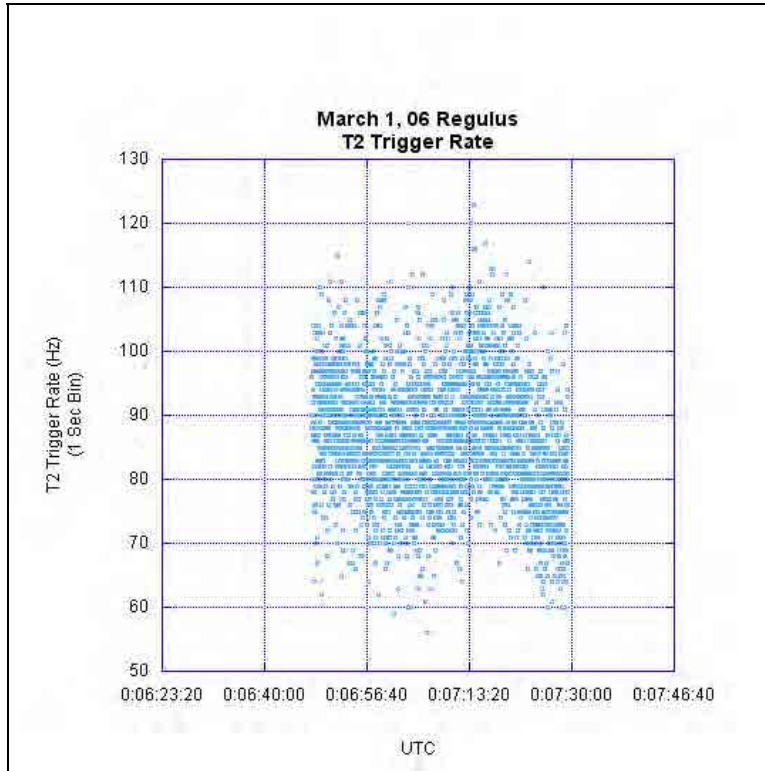

Figure 19: March 1, 06 T2 Trigger Rate

A boxcar average takes a number of points around each data point and averages them for each point. Therefore, the total number of data points does not change, but each data point is averaged over a longer period of time. As the number of points averaged is changed the correlation between the T2 trigger rate and the IR pyrometer changes. Figure 20 shows a graph of the number of points averaged and the correlation, *R*, between the T2 trigger rate and –IR temperature. The graph begins to flatten out between 20 and 30 points. Therefore, 25 points (or seconds) was chosen as the boxcar average size.
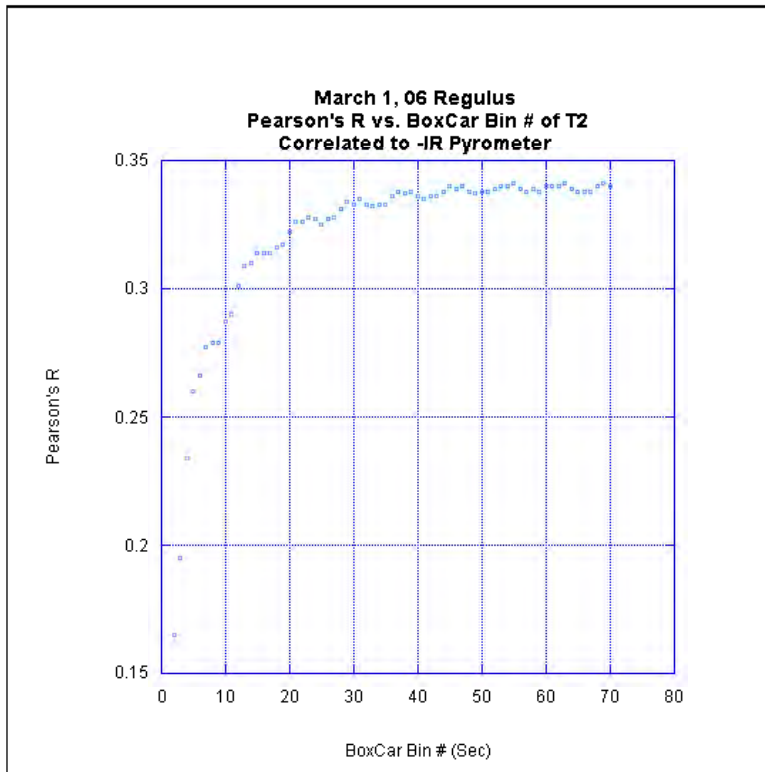
Figure 20: Pearson's R (of T2 vs IR Pyrometer) vs. Number of BoxCar Points

The maximum Pearson's correlation in Figure 20 is less than 0.35 due to omitted data points in IR temperature from the VI's dead times. The omitted values were set to zero, which skews the correlation. These data points are masked for calculating the *R* value shown in Figure 21.
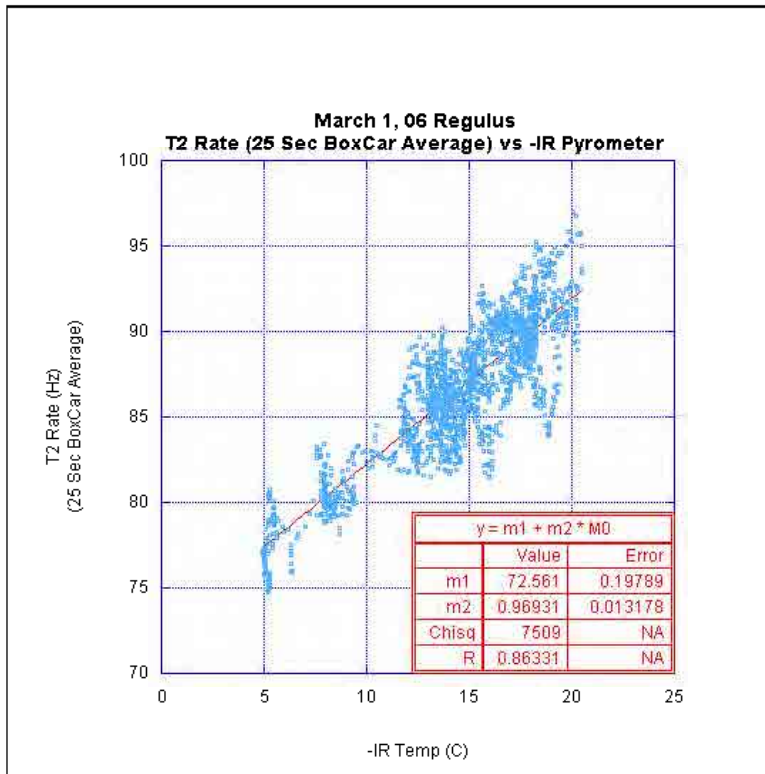
Figure 21: Pearson's R for T2 Correlated to IR Pyrometer

Figure 21 shows the correlation, *R*, for the T2 trigger rate versus –IR temperature.

The correlation between the IR pyrometer and the T2 trigger rate with a 25 second boxcar average is,
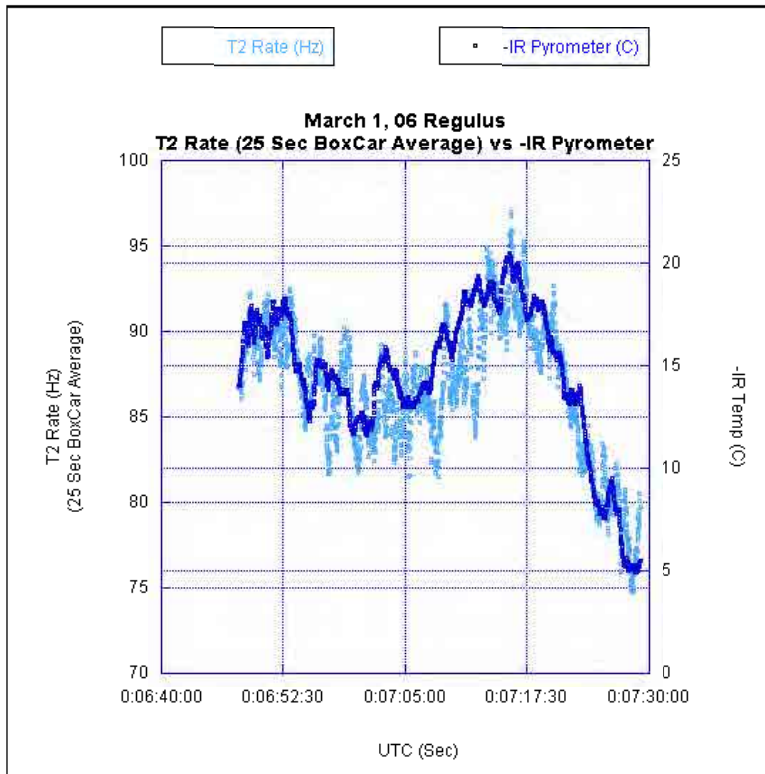
$$R = 0.86331.$$

Correlation is often referred to as R^2 to cancel negative signs,

$$R^2 = 0.74530.$$

Figure 22 show the T2 trigger rate with a 25 seconds boxcar average and –IR temperature versus UTC overlapped on the same graph. The boxcar average definitely improved the correlation between the two sets of data.

Figure 22: March 1, 06 T2 Trigger Rate and –IR Temperature

This correlation value is not as high as was expected. The correlation may be low due to many factors.

The data was not collected for as long as intended due to difficulties with the T2 telescope. This issue was resolved by the second night in which similar data was collected.

The height of the clouds may have also affected the data. The IR pyrometer will detect clouds at multiple altitudes with no indication of cloud height. If the clouds are above the Cherenkov radiation shower, the IR pyrometer may detect clouds that do not affect the trigger rate. Further research needs to be done to understand the significance of cloud height and possibly the ability to determine cloud height with the IR pyrometer.

Equation 6 assumes the relationship between the trigger rate and the IR pyrometer is linear. Due to the different types of scattering in the atmosphere (Rayleigh and Mie) the IR pyrometer and the T2 trigger rate should attenuate slightly differently due to wavelengths. This effect could be reduced by observing at a fixed elevation with constant atmospheric slant depth. This issue was addressed on the second night of collecting trigger rate and IR pyrometer correlation data.

b) March 3, 2006 L3 Trigger Rate vs. IR Pyrometer

March 5th was a very cloudy night for comparing the VERITAS trigger rate and the IR pyrometer. The level three trigger, L3, was used this night, meaning both VERITAS telescopes, T1 and T2, telescopes were working in stereo. Both VERITAS and the atmospheric monitoring Meade telescope were pointing at a fixed position, 90 [0] azimuth and 80 [0] altitude. This reduced any effects from changes in the depth of the atmosphere when tracking a source. The IR pyrometer was set to a 1 second response time and the L3 trigger rate data was stored in 1 second

bins. The UTC time was logged with both data sets such that the data could be compared. The dead time of the IR pyrometer VI's was greatly improved such that no data points were omitted from the IR pyrometer data sequence.

The following graphs show the results of March 5th. Data related to Figure 23, Figure 24, Figure 25, Figure 26, and Figure 27 are available at http://www.physics.utah.edu/~kwaller/Atmosphere/ under "Clouds vs. L3 Trigger Rate" data.

Figure 23 shows UTC time versus –IR temperature. The temperature resolution is 0.2 ^{0}C. The temperature error bars are not shown due to their relative size to the y-axis. The negative temperature was again used such that lower y-axis values indicate clouds.
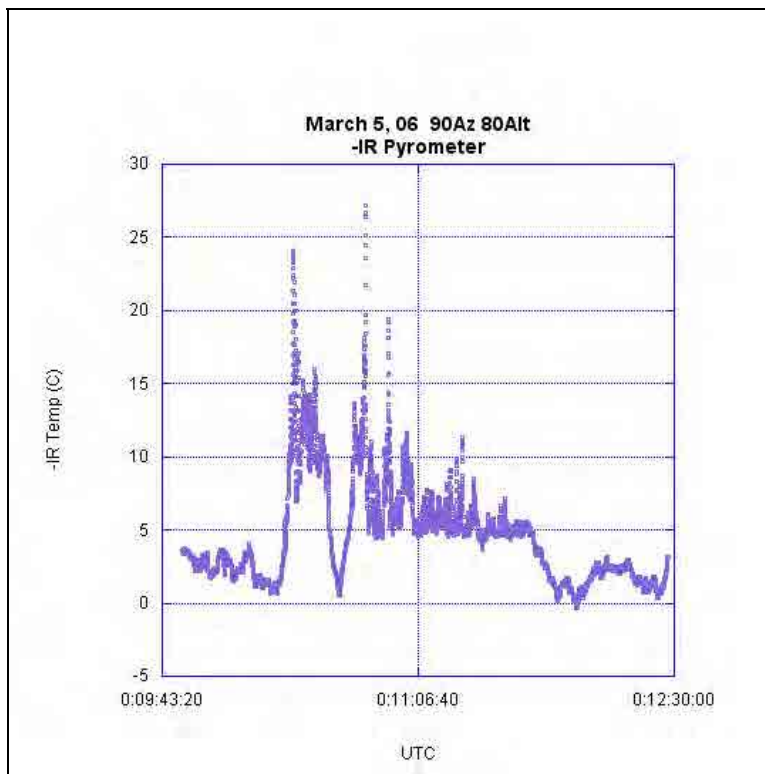
**Figure 23: March 5, 06 IR Pyrometer**

Figure 24 shows UTC time versus L3 trigger rate. The error in the L3 trigger rate is equal to the square root of the trigger rate. This error is approximately equal to the spread in the data points in the y-axis. A boxcar average was applied to the trigger rate data to reduce the spread in the points and show a better correlation to IR pyrometer.

33
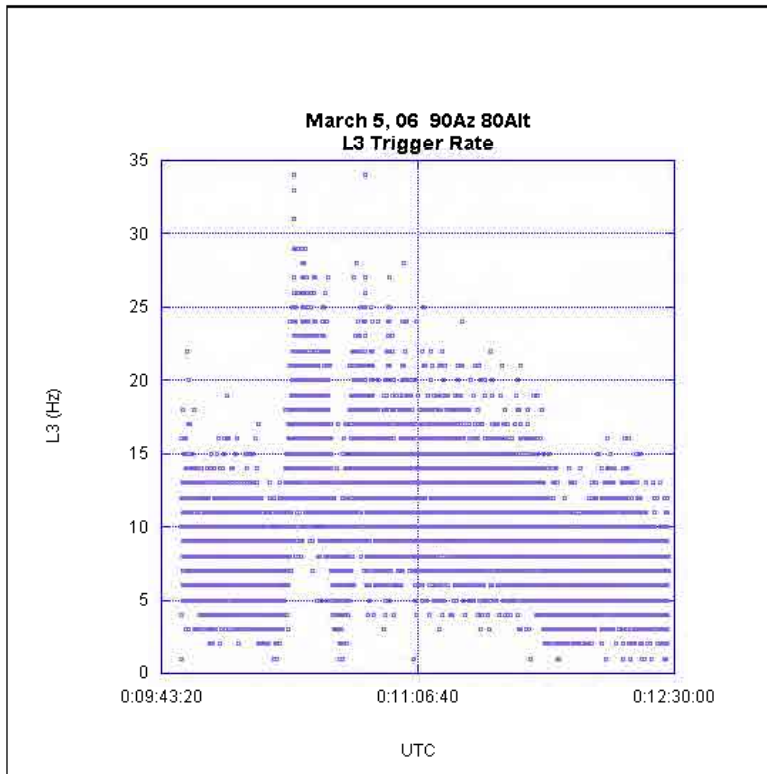
Figure 24: March 5, 06 L3 Trigger Rate

Figure 25 shows a graph of the number of points averaged and the correlation, *R*, between the L3 trigger rate and –IR temperature. Again, the graph begins to flatten out between 20 and 30 points. Therefore, 25 points (or seconds) was chosen as the boxcar average length.
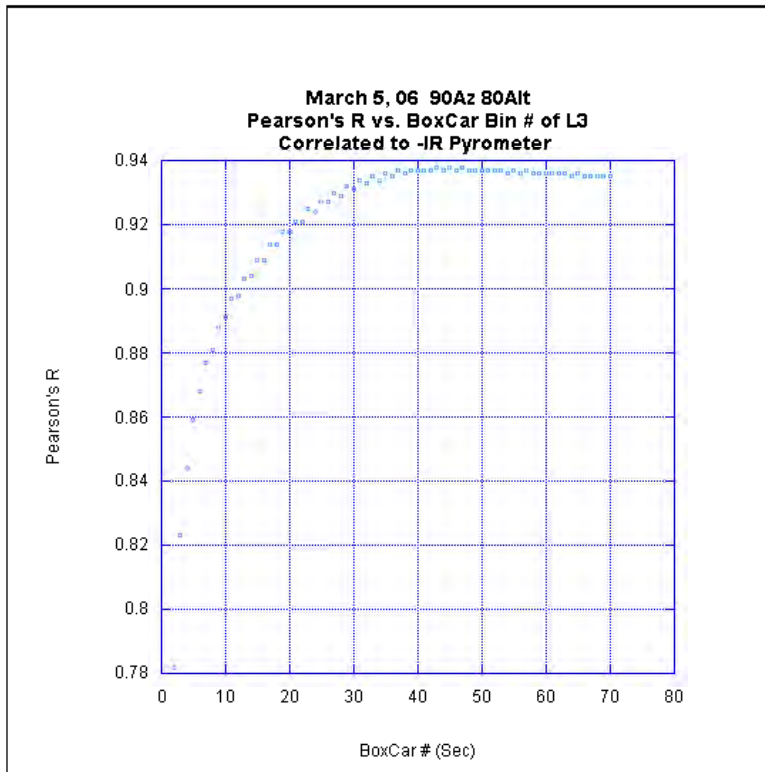
Figure 25: Pearson's R (of L3 vs. IR Pyrometer) vs. Number of BoxCar Points

Figure 26 shows the correlation, *R*, for the L3 trigger rate versus –IR temperature with the 25 second boxcar average.

      The correlation between the IR pyrometer and the L3 trigger rate is,

$$R = 0.92731.$$

$$R^2 = 0.85990.$$

Figure 27 shows the L3 trigger rate with a 25 seconds boxcar average and –IR temperature versus UTC overlapped on the same graph.
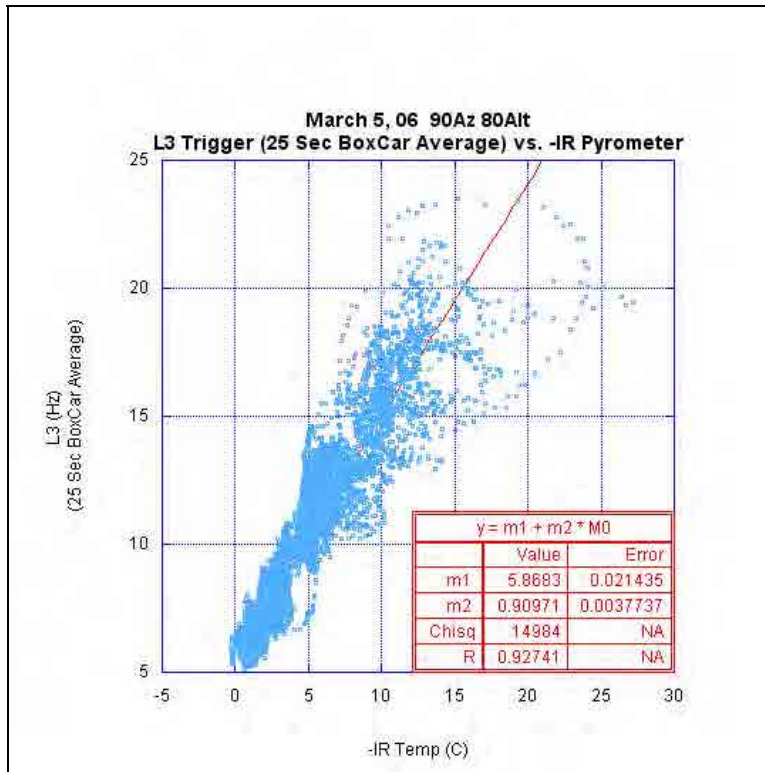
Figure 26: Pearson's R for L3 Correlated to IR Pyrometer

Figure 27: March 5, 06 L3 Trigger Rate and –IR Temperature

The correlation between the L3 trigger rate and the IR pyrometer is slightly better than the correlation between the T2 trigger rate and the IR pyrometer. One thing to notice in Figure 2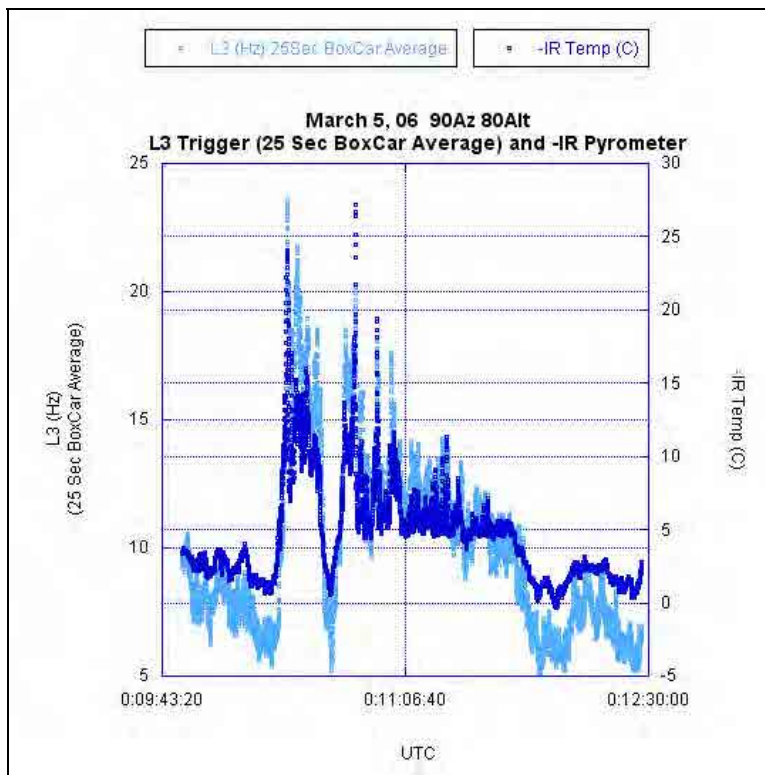7 is the decrease in correlation between the data points for low values on the y-axis. This may be due the trigger level used for L3. The trigger level was set lower than usual for this night due to the clouds. However, the trigger level may not have been set low enough to count rates corresponding to very low –IR temperature values.

Overall, there is a significant correlation between the IR pyrometer and the VERITAS cosmic ray trigger rate. Further work needs to be done to completely understand any small variations between the two measurements. Further work will hopefully involve installing one IR pyrometer on each VERITAS telescope. Further study may enable observers to correct the trigger rate for clouds based on IR pyrometer measurements.

B. Atmospheric Attenuation Using Star Intensity

The atmospheric attenuation length was only calculated for clear nights as determined by the IR pyrometer stability. See Appendix V for justification of using the IR pyrometer stability to choose which atmospheric attenuation data to be used for analysis.

The atmospheric attenuation length was calculated using star intensity. By choosing a relatively bright star, the intensity of the star is measured as it changes altitude and the change in intensity over altitude is used to calculate the atmospheric attenuation.

Multiple stars were chosen for collecting atmospheric attenuation data. All the stars were either types A, B, or O, meaning that they emitted light mostly in the blue part of the spectrum. It was important to use bright blue stars since VERITAS is most interested in the atmospheric attenuation in the blue and ultraviolet parts of the spectrum, where the Cherenkov radiation is the most intense. The stars were also selected based on altitude over the course of the night for the months of February and March. Sirius, Regulus, Spica, and Vega were the most often used. The best results, and all the data used for analysis were collected while observing Sirius. Sirius is a type A star with an absolute magnitude of 1.4.

The Meade LX 90 telescope was used to track the star. The telescope was aligned on the star using the "Easy, Two Star" alignment method outlined in the operating manual. The altitude of the star is reported by the Meade telescope and is considered exact since the telescope time is set to the computer time and the star is centered in the telescopes field of view.

The intensity of the star was measured using the CCD camera. The CCD exposure time was set at the minimum value of 0.12 seconds. Longer exposures of a bright star such as Sirius would result in saturation of the CCD pixels. All exposures were taken while the CCD camera was temperature regulated with the CCD setpoint at 1500. All exposures were taken at highest resolution, 1 X 1 pixels, to maximize the information about the star intensity.

Each CCD exposure was calibrated for electronic noise by subtracting a dark exposure. All dark exposures were 0.12 second exposures taken with the camera shutter left closed. Some of the dark exposures were taken while temperature regulated with the CCD setpoint at 1500. This is indicated in the data in Sec IV.B.2. Further analysis will need to be done to understand the

importance of temperature regulation for dark exposures. To reduce time between exposures, a master dark exposure was created at the beginning of the night. The master dark was an average of four to six dark exposures. All of the dark exposures taken in February and March were similar enough to indicate that dark exposures do not change significantly over the course of a month. Therefore, making one master dark exposure at the beginning of each night is more than adequate.

Since the dark exposures are consistent and the intensity of the star only needs to be relative to compute the atmospheric attenuation, it may seem unnecessary to do a dark subtraction. However, without a dark subtraction, the brightest pixels in the CCD image would be a result of electronic noise and not the star intensity. This would make it difficult to select a region of interest around the star based on pixel values.

Many CCD camera users often take flat exposures to reduce errors in a CCD image due to dust on the lens. Flat exposures are usually taken during daylight hours of either clear sky or a blank piece of paper. This produces an image of the dust in the camera and on the lens. Since dust speck in the images would be consistent and do not affect the relative intensity of the star, flat exposures were not needed.

All exposures were taken as rapidly as possible. Dead time between CCD exposures is attributed to the time it takes the computer to execute the VI, the IR pyrometer response time, rotating the color filter wheel, and reading data off of the CCD to the computer.

The filter wheel was rotated one position between each exposure in order to collect data for measuring atmospheric attenuation at all five filter wavelengths. The time is takes to read the data off the CCD depends on the number of pixels to be read. It is faster to dump unwanted pixels at the CCD than to read them out. By occasionally checking that the star is still centered in the CCD image it is possible to only read out 50 or so horizontal lines surrounding the star. This dramatically reduces the time between exposures from about 30 seconds to readout the full CCD to less than 7 seconds in some instances. To further improve readout time, it would help to not readout each horizontal line completely. This would require further optimization of the readout capabilities of the CCD camera.

1. Determine Star Intensity

Quantifying the intensity of a star was more difficult than originally expected. The intensity of a star can not be defined by a single pixel even though a star is very close to a point source to a ground observer. Due to aberration in the atmosphere and the optics of the CCD camera, the star may take up a few or a few dozen pixels depending on the filter wavelength. Therefore, it is best to analyze a region of interest (ROI) centered on the star. The brightest pixel is used to indicate the center of the star in the CCD image. The brightest pixel is easily selected if the image has been properly dark subtracted. For my analysis, I arbitrarily choose to select a 40 X 40 pixel ROI. Further work may involve selecting larger and smaller regions of interest.


Figure 28: Example of Data Readout and Highlighted ROI

Figure 29, Figure 30, and Figure 31 are histograms of 40 X 40 pixel ROIs taken of Sirius. The large number of pixels with low intensities is due to the background area in the ROI. The small distribution toward the right is due to the star. This distribution is composed of very few pixels and does not fit well to a Gaussian distribution. The distribution is not expected to be Gaussian since the CCD camera lens does not focus perfectly for all filter wavelengths. A slightly out of focus star will often resemble more of a donut than a Gaussian distribution. Therefore, it is more effective to analyze the distribution by summing the pixels composing the star in the ROI.
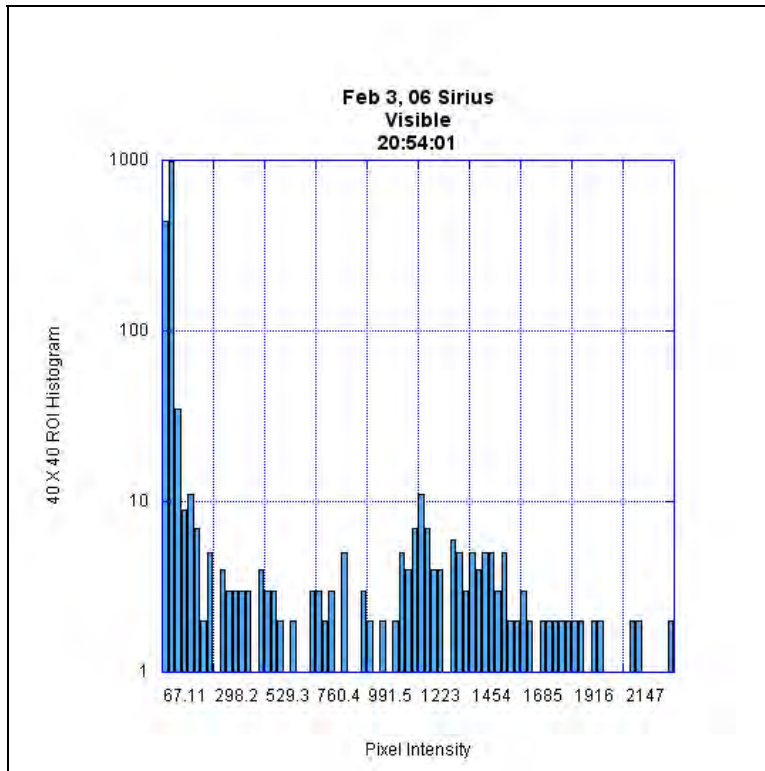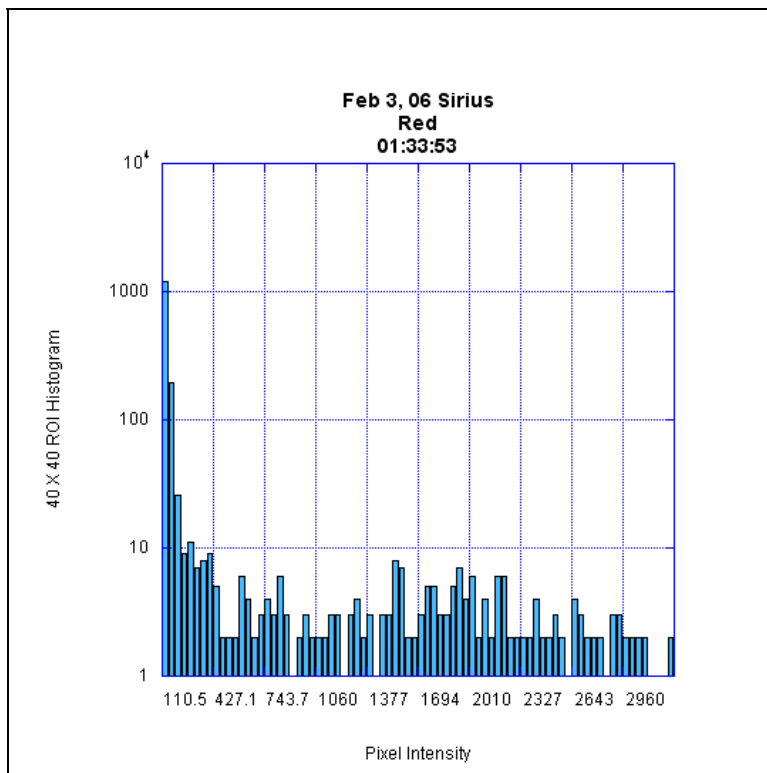

Figure 29: 40 X 40 ROI Histogram with Visible Filter
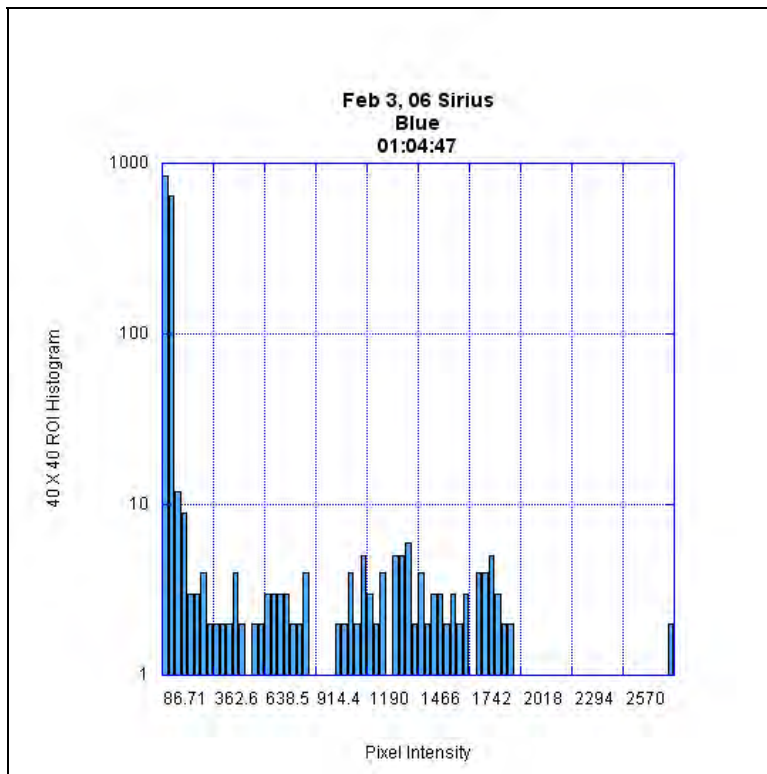
Figure 30: 40 X 40 ROI Histogram with Blue Filter

Figure 31: 40 X 40 ROI Histogram with Red Filter

The difficult part in quantifying star intensity was separating the pixel contribution due to the star from the contributions due to background pixels. Since the number of pixels due to the background is very large, the mean pixel value of the ROI is essentially the mean pixel value of the background and the standard deviation from the mean is approximately the standard deviation in the background pixels. Therefore, the star pixels may be separated from the background by ignoring all pixels below a number of standard deviations from the background or average.

The overall background intensity of each CCD image fluctuates slightly due to the either the moon or facility at the observation site. For data collected on March 1st, each 40 X 40 ROI was background subtracted with an equal sized ROI from a star-free region of the image. To more accurately model the background image it would be better to use the background of the entire CCD image (765 X 510 pixels). This would require rescaling the (765 X 510) background to match the size of the ROI. This may be used in future work. The new ROI is referred to in my data as "40 X 40 ROI-Background". There were not enough clear nights after March 1st to analyze the impact of doing a background subtract.

For each observation night, the data collected was logged in both raw format, and in calculated star intensities. Pixels below 1 to 6 standard deviations of the mean were ignored in calculating the star intensities. By graphing the data (intensity and altitude) for each color filter position and computing the correlation, the best definition of intensity was defined for each filter per night. For example, for the night of February 3, the most accurate measurement of atmospheric attenuation in the ultraviolet was computed by defining the star intensity as,

$$\textit{Star Intensity} = \Sigma \textit{ Pixels above 3 Standard Deviations of the Mean.}$$

The methods used to define the star intensity in the analyzed data per filter for each night are indicated in the following section.

2. Atmospheric Attenuation Measurements

Data from the nights of February 1st, February 3rd, February 24th, and March 1st were used to calculate atmospheric attenuation. These nights were all very clear with the exception of part of the night of February 24th. Data collected on February 24th was easily modified by removing data points corresponding to IR pyrometer readings with strong variability. All data was collected by analyzing Sirius. Sirius consistently gave the best results due to the large change in altitude observable during the night.

a) February 1st 2006

February 1st was one of the first nights for collecting atmospheric attenuation data. It served mostly as a test run but proved to be adequate for analysis. This was important since most of the subsequent observation nights were too cloudy to acquire useful data. The data was not background subtracted and the dark exposures were not temperature regulated. These details were not considered until later observations. The moon was not up for any part of this observation, which fortunately reduced background fluctuations in the overall intensity measurement.

Since February 1st was only supposed to be a test run, only the ultraviolet filter was used. The intensity of each exposure was defined as the maximum pixel value in the CCD image. This definition of intensity was not accurate but worked well enough this night for analysis.

At various times of the night, the ambient temperature and humidity was logged for any future analysis. Changes in atmospheric attenuations may be related to ambient temperature and humidity.
All temperature and humidity data was accessed from a weather monitoring station in Tucson Arizona.

- @9:53 pm 12 ^{0}C 33% H
- @12:05 am 7 ^{0}C 39% H
- @1:07 am 6 ^{0}C 46% H
- @2:50 am 4 ^{0}C 46% H

The plotted results of February 1st are given in Appendix I. The slope of *M0=1/sin(θ)* versus *y=ln(I)* is,

$$m2 = -0.445 \pm 0.013$$

The error in the slope is due to the residuals of the linear least square fit.

b) February 3rd 2006

Data collected February 3rd was not background subtracted and the dark exposures were not temperature regulated. A very small crescent moon was up for the first half of the run but was approximately 50 ^{0} distant from Sirius.
    The intensity of the star was defined by the sum of the pixels above N standard deviations of the ROI mean, where N for each filter is;

- UV N = 3
- Blue N = 4
- Visible N = 4
- Red N = 4
- IR N = 3

The ambient temperature and humidity was logged at various times of the night.

- @8:50 pm 16 ^{0}C 27% H
- @11:03 pm 9 ^{0}C 40% H
- @2:54 am 8 ^{0}C 40% H

The plotted results of February 3rd are given in Appendix II. The slopes of *M0=1/sin(θ)* versus *y=ln(I)* for each filter are,

Table 2: February 3rd Attenuation Slopes

Filter	Slope = m2
UV	-0.364 ± 0.013
Blue	-0.2109 ± 0.0049
Visible	-0.0769 ± 0.0028
Red	-0.0519 ± 0.0026
IR	-0.0250 ± 0.0021

The errors in the slopes are due to the residuals of the linear least square fits.

c) February 24th 2006

Data collected February 24th was not background subtracted. The dark exposures were temperature regulated at a setpoint of 1500. The moon was not up during the run.

The intensity of the star was defined by the sum of the pixels above N standard deviations of the ROI mean, where N for each filter is;

- o UV N = 2
- o Blue N = 5
- o Visible N = 3
- o Red N = 3
- o IR N = 5

The ambient temperature and humidity was logged at various times of the night.

- @8:55 pm 14 ^{0}C 21% H
- @9:55 pm11 ^{0}C 24% H
- @11:55 pm 8 ^{0}C 25% H
- @12:55am 8 ^{0}C 25% H

The plotted results of February 24th are given in Appendix III. The slopes of *M0=1/sin(θ)* versus *y=ln(I)* for each filter are,

Table 3: February 24th Attenuation Slopes

Filter	Slope = m2
UV	-0.417 ± 0.021
Blue	-0.2935 ± 0.0072
Visible	-0.1738 ± 0.0061
Red	-0.1205 ± 0.0062
IR	-0.0584 ± 0.0066

The errors in the slopes are due to the residuals of the linear least square fits.

d) March 1st 2006

Data collected March 1st was background subtracted. The dark exposures were temperature regulated at a setpoint of 1500. The moon was not up during the run.

The intensity of the star was defined by the sum of the pixels above N standard deviations of the ROI mean, where N for each filter is;

- o Ultraviolet N = 5
- o Blue N = 4
- o Visible N = 3
- o Red N = 3
- o Infrared N = 5

The ambient temperature and humidity was logged at various times of the night. The humidity was significantly higher on March 1st.

- @7:55 pm 16 C 68% H
- @10:55 pm12 C 72% H
- @11:55 pm11 C 71% H

The plotted results of March 1st are given in Appendix IV. The slopes of *M0=1/sin(θ)* versus *y=ln(I)* for each filter are,

Table 4: March 1st Attenuation Slopes

Filter	Slope = m2
UV	-0.442 ± 0.016
Blue	-0.1883 ± 0.0054
Visible	-0.0894 ± 0.0039
Red	-0.0528 ± 0.0037
IR	-0.032 ± 0.0035

The errors in the slopes are due to the residuals of the linear least square fits.

e) Average Atmospheric Attenuation

Table 5 is a summary of the slopes calculated for each analyzed observation.

Table 5: Attenuation Slopes by Date
y = Ln (Intensity), M0 = 1/Sin(θ)

Date	Filter	Slope = m2
2/1/2006	UV	-0.445 ± 0.013
2/3/2006	UV	-0.364 ± 0.013
2/3/2006	Blue	-0.2109 ± 0.0049
2/3/2006	Visible	-0.0769 ± 0.0028
2/3/2006	Red	-0.0519 ± 0.0026
2/3/2006	IR	-0.0250 ± 0.0021
2/24/2006	UV	-0.417 ± 0.021
2/24/2006	Blue	-0.2935 ± 0.0072
2/24/2006	Visible	-0.1738 ± 0.0061
2/24/2006	Red	-0.1205 ± 0.0062
2/24/2006	IR	-0.0584 ± 0.0066
3/1/2006	UV	-0.442 ± 0.016
3/1/2006	Blue	-0.1883 ± 0.0054
3/1/2006	Visible	-0.0894 ± 0.0039
3/1/2006	Red	-0.0528 ± 0.0037
3/1/2006	IR	-0.0320 ± 0.0035

*Errors in Slopes are due to Residual of the Fits

Table 6 shows the average atmospheric attenuation lengths assuming the thickness of the atmosphere at the observation site is 1000 km – 1.275 km = 998.725 km.

Table 6: Average Slopes and Attenuation Lengths
Thickness of Atmosphere at Sea Level = 1000 km, T_0 = 998.725 km

Filter	Average Slope	Attenuation Length (km)
UV	-0.417 ± 0.024	2410 ± 139
Blue	-0.231 ± 0.032	4480 ± 621
Visible	-0.113 ± 0.031	9968 ± 2735
Red	-0.075 ± 0.023	13316 ± 4084
IR	-0.038 ± 0.011	23282 ± 6740

The errors in the average slopes were calculated using both the errors in the averaged values and the spread in the averaged values. The spread in the averaged values was used to calculate standard error,

$$\sigma_{\bar{x}} = \frac{\sigma_x}{\sqrt{N}} = \frac{\sqrt{\frac{1}{N-1}\sum(x_i - \bar{x})^2}}{\sqrt{N}} \;,$$

Equation 7: Standard Error

where N is number of points averaged and σ_x is the standard deviation. The average error in the individual slopes and the standard error were added in quadrature to determine the errors in the average slopes.

Simple error propagation was used to calculate the errors in the atmospheric attenuation lengths, $S_{attenuation}$, from the errors in the average slopes, S_{slope},

$$\left(\frac{S_{attenuation}}{attenuation}\right)^2 = \left(\frac{S_{slope}}{slope}\right)^2 .$$

Equation 8: Error in Atmospheric Attenuation

Error in the atmospheric depth at zenith at the observation site was not used in calculating the error in atmospheric attenuation.

Table 7 shows the average atmospheric attenuation lengths assuming the thickness of the atmosphere is defined as containing 99% of the atmosphere. Therefore, the thickness of the atmosphere at the observation site is 31 km – 1.275 km = 29.725 km.

Table 7: Average Slopes and Attenuation Lengths
Thickness of Atmosphere Containing 99% = 31 km, T_0 = 29.725 km

Filter	Average Slope	Attenuation Length (km)
UV	-0.417 ± 0.024	71.3 ± 4.1
Blue	-0.231 ± 0.032	129 ± 18
Visible	-0.113 ± 0.031	263 ± 72
Red	-0.075 ± 0.023	396 ± 121
IR	-0.038 ± 0.011	782 ± 226

Table 8 shows the average atmospheric attenuation assuming the atmospheric pressure at the observation site is 815.5 g/cm^2.

Table 8: Average Slopes and Attenuation Lengths
Atmospheric Pressure = T_0 = 815.5 g/cm^2, $\rho_{sea\ level}$ = 1.2 x 10^3 g/cm^3

Filter	Average Slope	Attenuation (g/cm^2)	Attenuation Length (km)
UV	-0.417 ± 0.024	1956 ± 113	16.3 ± 0.9
Blue	-0.231 ± 0.032	3530 ± 489	29.4 ± 4.1
Visible	-0.113 ± 0.031	7216 ± 1980	60 ± 16
Red	-0.075 ± 0.023	10873 ± 3334	91 ± 28
IR	-0.038 ± 0.011	21461 ± 6994	179 ± 58

f) Discussion

The most notable pattern in the atmospheric attenuation is a decrease in atmospheric attenuation length toward the infrared end of the spectrum. This is consistent with Rayleigh scattering. The intensity of Rayleigh scattering is proportional to λ^{-4}.

$$\lambda_{Blue} = 435 \text{ nm,} \qquad \lambda_{UV} = 365 \text{ nm,}$$
$$\lambda_{Red} = 600 \text{ nm,} \qquad \lambda_{IR} = 780 \text{ nm,}$$
$$(435/600)^{-4} = 3.6 \qquad (365/780)^{-4} = 20.9$$

Blue light should be scattered 3.6 times more than red light and ultraviolet light should be scattered 20.9 times more than infrared light. Therefore, the attenuation length measured with the red filter should be 3.6 times that of the blue filter and the attenuation length measured with the infrared filter should be 20.9 times that of the ultraviolet filter. The average atmospheric attenuation length due to the red filter is 3.08 times greater than that of the blue filter. The average atmospheric attenuation length due to the infrared filter is 58.4 times greater than that of the ultraviolet filter.

The percent differences between expected and calculated differences are:

14.4% for comparing the blue and red filters,
179% for comparing the ultraviolet and infrared filters.

Therefore, the difference in atmospheric attenuation for visible light is mostly due to Rayleigh scattering. The difference in atmospheric attenuation between ultraviolet and infrared is due to Rayleigh scattering and significant Mie scattering off large particles toward the infrared end of the spectrum. The large discrepancy in the difference between ultraviolet and infrared my also be partly attributed to the large percent error in the attenuation length in the infrared.

Since atmospheric attenuation lengths change with weather conditions, there are no accepted values to compare this data with. However, comparisons can be made to data collected by former VERITAS member, Gary Walker. His data most resembles the atmospheric attenuation lengths calculated by assuming the depth of the atmosphere is defined as containing 99% of the atmosphere or using atmospheric pressure and density. This is a good indication that the atmospheric depth at zenith should not be defined as 1000 km at sea level. This depth was derived from the ability to detect any particles constituting atmosphere. Table 9 and Figure 32 show the measured attenuation lengths compared to Walker's data. The attenuation lengths calculated using atmospheric pressure and density are slightly more in agreement with Walker's results.[xx]

Table 9: Measured Attenuation Lengths and Gary Walker's Results

Filter	Attenuation Length (km) 99% = 31 km T_0 = 29.725 km	Attenuation Length (km) T_0 = 815.5 g/cm^2 $\rho_{sea\ level}$ = 1.2 x 10^3 g/cm^3	Attenuation Length (km) Gary Walker's Data
Ultraviolet	71.3 ± 4.1	16.3 ± 0.9	21.84
Blue	129 ± 18	29.4 ± 4.1	39.81
Visible	263 ± 72	60 ± 16	84.03
Red	396 ± 121	91 ± 28	134.7
Infrared	782 ± 226	179 ± 58	44.91
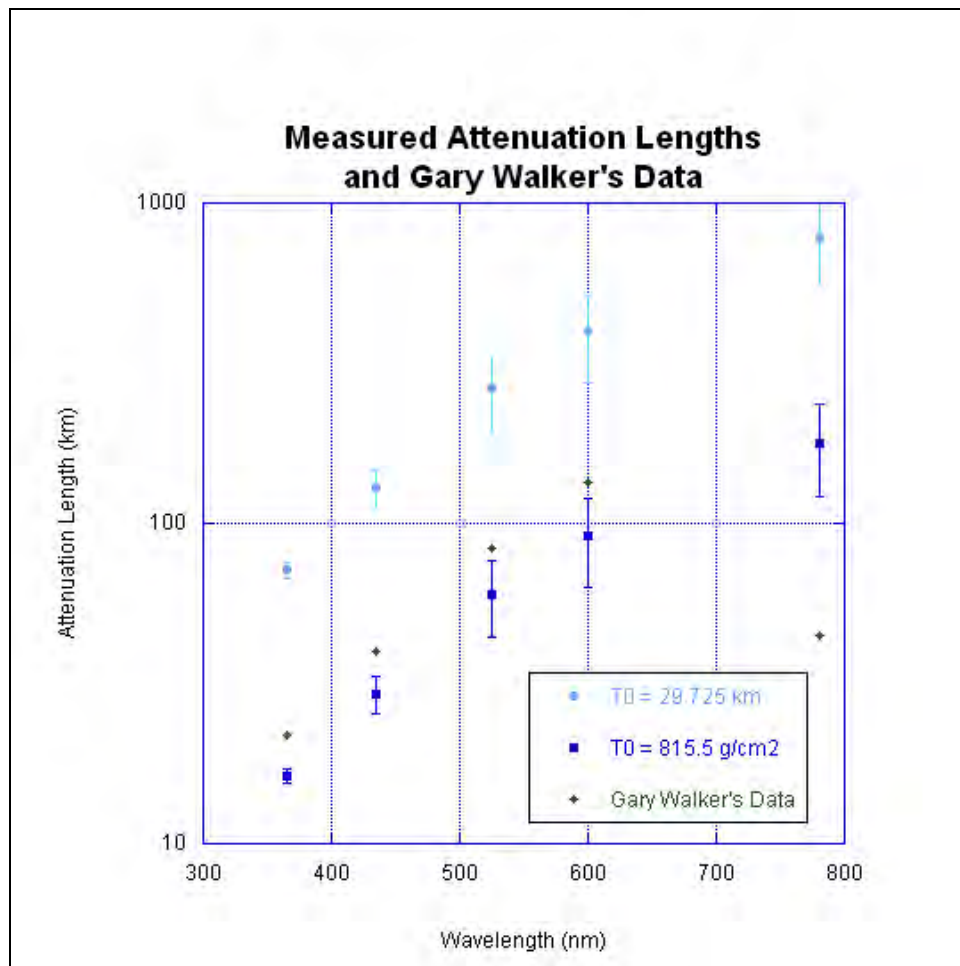
Figure 32: Measured Attenuation Lengths and Gary Walker's Results

Using ideal weather conditions, it is possible to calculated expected attenuation lengths due to Rayleigh scattering. Table 10 shows expected values for attenuation lengths, taken from Burle Industries', *Electro-Optics Handbook*[xxi]. These values were calculated for horizontal transmission at sea level in a model clear standard atmosphere.

Table 10: Expected Attenuation Lengths due to Rayleigh Scattering

Filter	Pass Band Center (nm)	Rayleigh Coefficient (km^{-1})*	Rayleigh Attenuation (km)
Ultraviolet	365	0.065 ± 0.002	15.4 ± 0.5
Blue	435	0.028 ± 0.002	35.7 ± 0.1
Visible	525	0.013 ± 0.001	77 ± 6
Red	600	0.0080 ± 0.0005**	125 ± 8
Infrared	780	0.0032 ± 0.0002**	313 ± 20

*Errors in Coefficients are based on the ability to read values in the *Electro-Optics Handbook*.
**Red and infrared coefficients are derived by extrapolating the data given in the *Electro-Optics Handbook*.
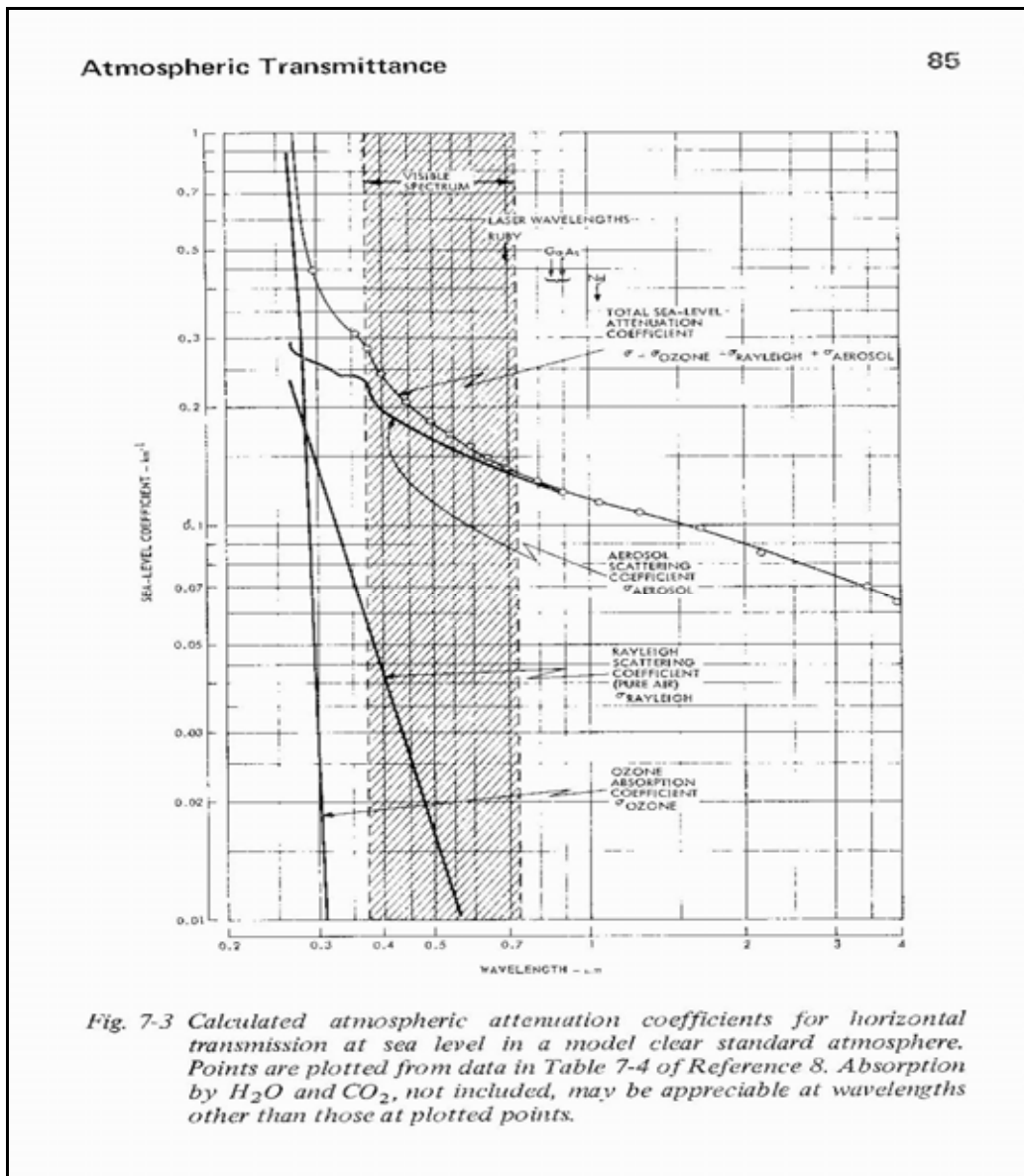
Figure 33: Expected Attenuation Coefficient from the *Electro-Optics Handbook*[xxii]

Figure 33 shows a graph of sea-level attenuation coefficients due to ozone, aerosols, and Rayleigh scattering. The attenuation coefficients due to Rayleigh scattering are extrapolated to red and infrared wavelengths and are used to calculate upper limits for atmospheric attenuation lengths.

Table 11 and Figure 34 show the measured attenuation lengths using atmospheric pressure and density compared to expected upper limits due to Rayleigh scattering.

Table 11: Measured Attenuation Lengths and Expected Upper Limits

Wavelength (nm)	Attenuation Length (km) $T_0 = 815.5$ g/cm^2 $\rho_{sea\ level} = 1.2 \times 10^3$ g/cm^3	Attenuation Length (km) Expected Upper Limit
365	16.3 ± 0.9	15.4 ± 0.5
435	29.4 ± 4.1	35.7 ± 0.1
525	60 ± 16	77 ± 6
600	91 ± 28	125 ± 8
780	179 ± 58	313 ± 20
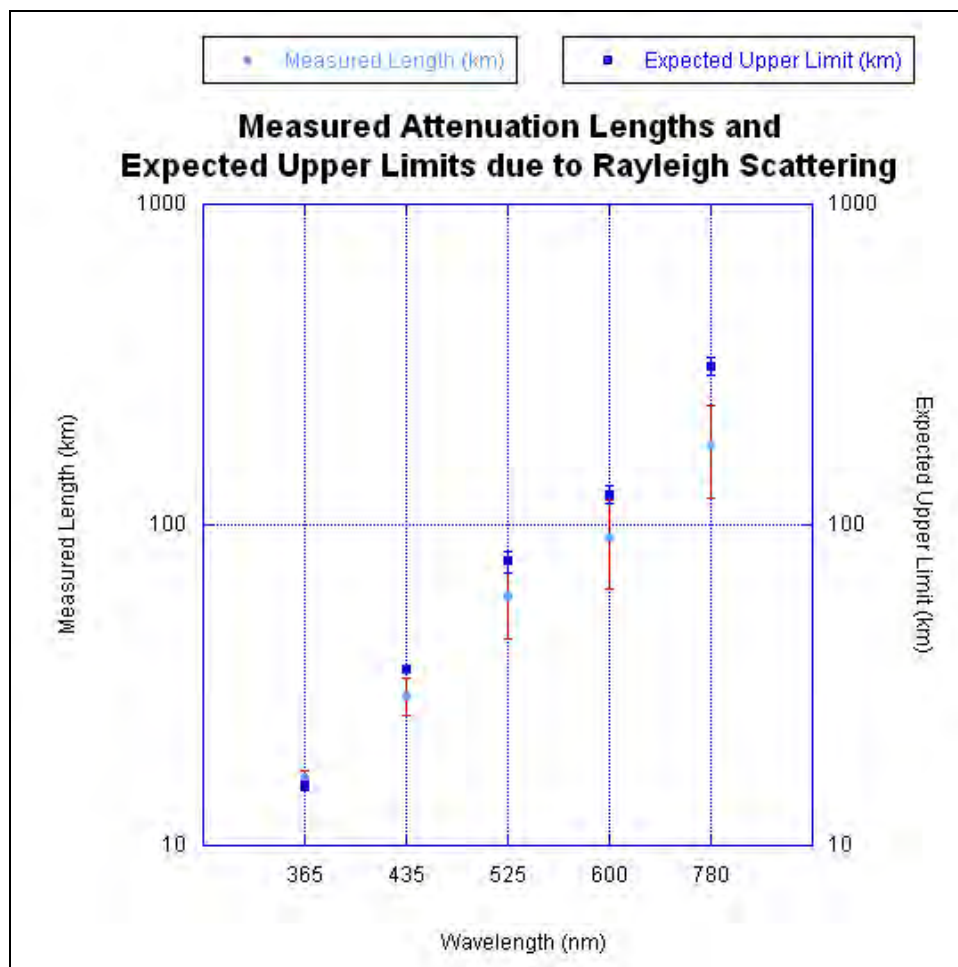
Figure 34: Measured Attenuation Lengths and Expected Upper Limits due to Rayleigh Scattering

Atmospheric attenuation is due to Rayleigh scattering and Mie scattering due to aerosols and ozone. Therefore, measured values for atmospheric attenuation should be shorter than the expected upper limit values given in Table 11. The measured values in Table 11 are greater than the expected attenuation lengths due to Rayleigh scattering. The difference in measured and expected upper limit values increases towards the infrared end of the spectrum. This increase is due to Mie scattering. Mie scattering has very little effect on ultraviolet radiation and a significant effect on infrared radiation. Therefore, the expected attenuation length for ultraviolet is very close to my measured value, and the expected attenuation length for infrared is not close to my measured value.

V. Recommendations

Many recommendations for improvements and extensions have already been noted in this document. Here are some further improvements to consider and possible extensions to the work already done.

A. Improvements

Many of the errors in the calculated atmospheric attenuation lengths are relatively large. The errors in the attenuation lengths may be related to the methods used to define star intensity. The most accurate measurement of atmospheric attenuation was a result of defining the star intensity as,

Star Intensity = Σ Pixels above N Standard Deviations of the Mean.

The definition of star intensity may be improved by dividing the intensity of the star by the number of pixels in the sum. This may reduce the spread in the data due to the change in the number of pixels in the sum.

The error in the atmospheric attenuation data becomes larger towards the red and infrared end of the spectrum. Future work may show that atmospheric attenuation measurements in the red and infrared are not relevant to the mostly ultraviolet sensitive VERITAS telescopes. It may be possible to omit collecting data in the red and infrared. This would allow for more data collection in the blue and ultraviolet. By not measuring in the red and infrared, it is possible to use a different CCD camera lens with a greater sensitivity to ultraviolet.

The systematic errors in the calculated atmospheric attenuation lengths are not known and significant due to the lack of a concrete definition of the depth of the atmosphere at zenith. A method used by former VERITAS member, Gary Walker, may resolve this issue. By knowing the change in elevation between the observation site and a second observation site, the atmospheric attenuation may be calculated by knowing the change in the slopes of $x = 1/Sin(\theta)$ and $y = ln(I)$. This method would do away with the need to know the depth of the atmosphere at zenith. However, this method would involve a second monitoring system at a second observation site.

B. Extensions

1. Cloud Detection

Section II.C briefly mentioned that there is not absolute scale of cloud coverage. Clouds are detected by observing an increase in the IR pyrometer temperature reading compared to clear sky. The scale is not absolute due to changes in humidity and ambient temperature over the course of the season.

It may be possible to establish an absolute scale for cloud coverage by studying the effects of temperature and humidity on the IR pyrometer readings. By monitoring the humidity and ambient temperature during several observations it may be possible to define a relationship between humidity and IR pyrometer readings and between ambient temperature and IR pyrometer readings. If this can be done, we could establish an absolute scale for cloud coverage.

2. Clouds vs. Trigger Rate

As shown in Figure 20 and Figure 25, both the T2 and the L3 cosmic ray trigger rates were best correlated to the IR pyrometer when the trigger rate data were adjusted with a 20 to 30 second boxcar average. More data needs to be collected to confirm 20 to 30 seconds is consistent for always correlating the trigger rate and the IR pyrometer. Further research needs to be done to understand why the data is best correlated between 20 and 30 seconds.

Section II.C briefly mentioned the issue of cloud height. As long as the Cherenkov radiation is produced above the clouds, the IR pyrometer and trigger rate should be correlated. If the Cherenkov radiation shower is produced below the clouds, the trigger rate my not change in the presence of clouds detected by the IR pyrometer. A method of detecting cloud height and Cherenkov radiation height may need to be investigated to fully correlate the trigger rate to the IR pyrometer temperature.

3. Atmospheric Attenuation Measurements

Atmospheric attenuation lengths are not constant over the course of a year. Changes in wind speed, ambient temperature, humidity, and dust can all affect attenuation length. Therefore, atmospheric attenuation lengths need to be measured over a long period of time to determine the relationship of atmospheric attenuation to changing weather conditions.

VI. Conclusion

The atmospheric conditions during observations at VERITAS are simple given an A, B, C, or D grade determined visually by observers at the beginning of each night. The atmospheric monitoring system provides VERITAS with a more quantitative description of atmospheric conditions by detecting clouds and measuring atmospheric attenuation.

Clouds are detected with an infrared radiation pyrometer. IR pyrometer data is correlated to the VERITAS cosmic ray trigger rate. The correlation is optimized by adjusting the trigger rate data with a 25 second boxcar average.

The correlation between the IR pyrometer and the trigger rate of VERITAS telescope number two is,

$$R = 0.86331,$$

$$R^2 = 0.74530 = 74.5\%.$$

The correlation between the IR pyrometer and the level three trigger rate of both VERITAS telescopes is,

$$R = 0.92731,$$

$$R^2 = 0.85990 = 86.0\%.$$

By correlating the VERITAS cosmic ray trigger rate to the IR pyrometer, it may be possible to use the IR pyrometer to adjust the VERITAS trigger rate to account for cloud coverage.

The atmospheric monitoring system measures attenuation by observing change in star intensity over varying atmospheric slant depths. The atmospheric attenuation length is calculated for multiple wavelengths; ultraviolet, blue, visible, red, and infrared.

Atmospheric attenuation lengths are calculated using the atmospheric pressure and density at sea level.

Table 12: Attenuation Lengths
Atmospheric Pressure = T_0 = 815.5 g/cm^2, $\rho_{sea\ level}$ = 1.2 x 10^3 g/cm^3

Filter	Attenuation (g/cm^2)	Attenuation Length (km)
UV	1956 ± 174	16.3 ± 0.9
Blue	3530 ± 841	29.4 ± 4.1
Visible	7216 ± 3385	60 ± 16
Red	10873 ± 5654	91 ± 28
IR	21461 ± 10166	179 ± 58
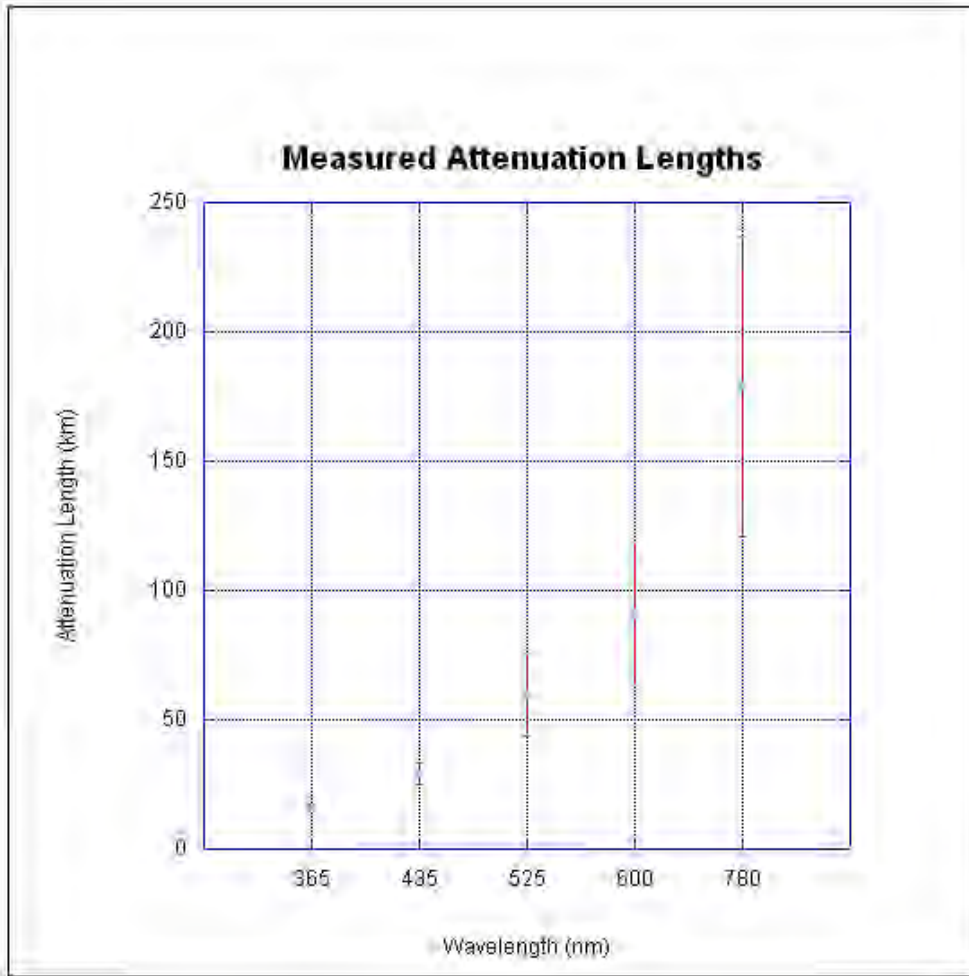
Figure 35: Attenuation Lengths

Future work may involve using calculated atmospheric attenuation to adjust cosmic ray trigger rate data to account for changes in altitude of gamma ray sources.

The project was a success. All the equipment is working. Atmospheric attenuation was measured. The IR pyrometer is highly correlated to the VERITAS trigger rate. Extensions and improvements to the project will be addressed this summer.

Acknowledgements

- David Kieda for his abundance of guidance on this project
- Stephan Lebohac for great suggestions on interfacing and analysis
- Peter Cogan for collecting VERITAS trigger rate data to compare to the infrared pyrometer
- Gary Walker for providing documentation on his work already done on this project
- Brian Grefenstette for help in interfacing to the Meade LX90 telescope mount
- Ken Gibbs for his assistance in analyzing the intensity of a star
- Jason Case of National Instruments for debugging interface code
- VERITAS members involved in the development of the atmospheric monitoring system

Appendix I. February 1st 2006 Graphs

Data related to Figure 36, and Figure 37 is available at
http://www.physics.utah.edu/~kwaller/Atmosphere/ .
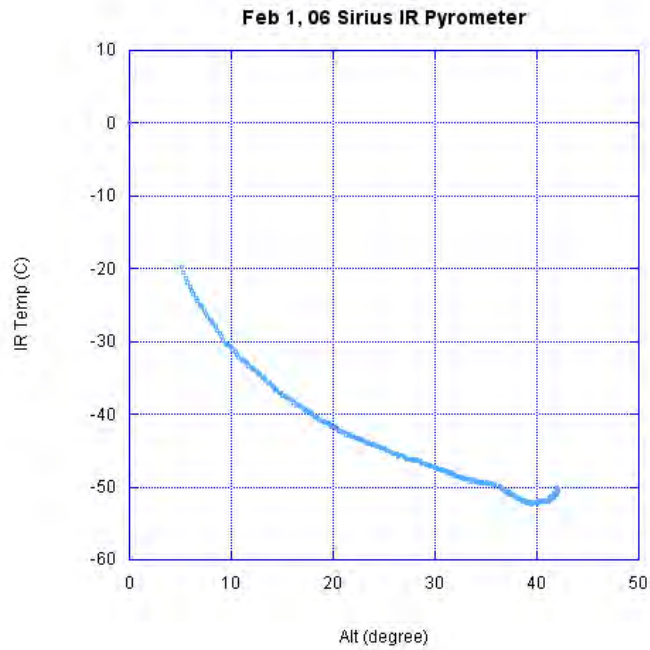
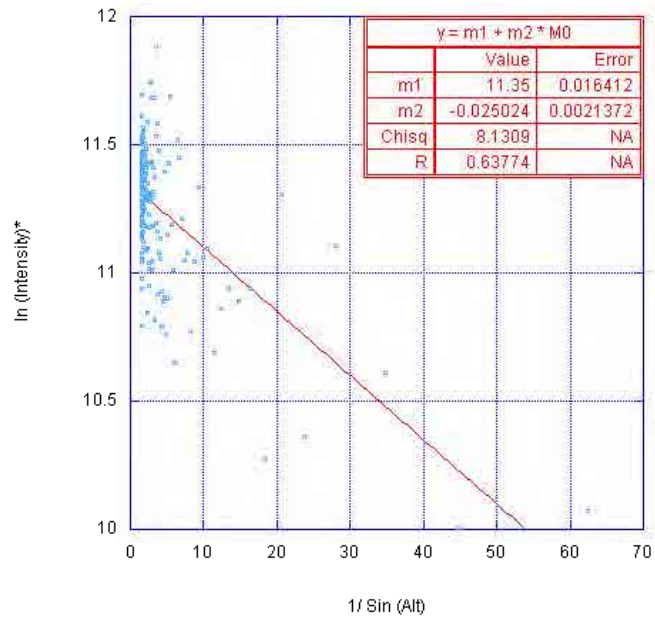
Figure 36: Feb 1, 06 IR Pyrometer
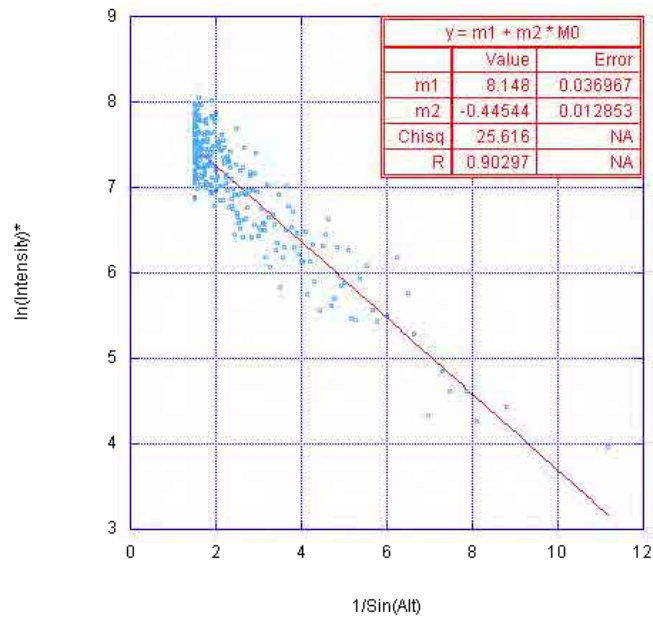
Figure 37: Feb 1, 06 UV Filter

Appendix II.   February 3rd 2006 Graphs

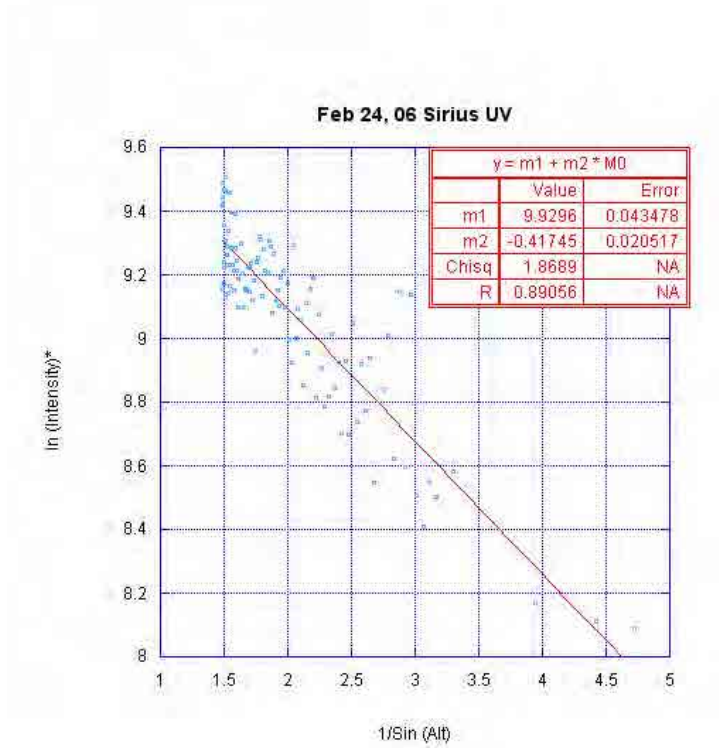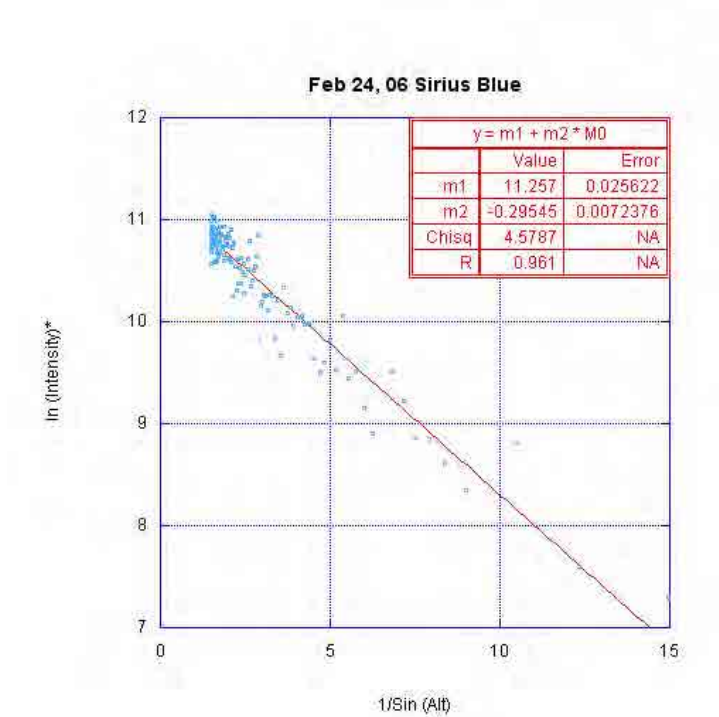Data related to Figure 38, Figure 39, Figure 40, Figure 41, Figure 42, and Figure 43 is available at http://www.physics.utah.edu/~kwaller/Atmosphere/ .
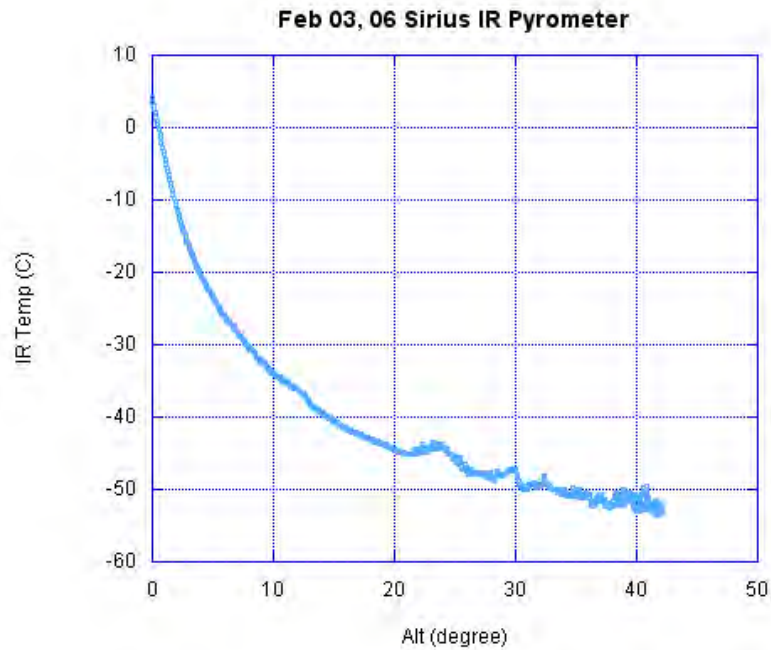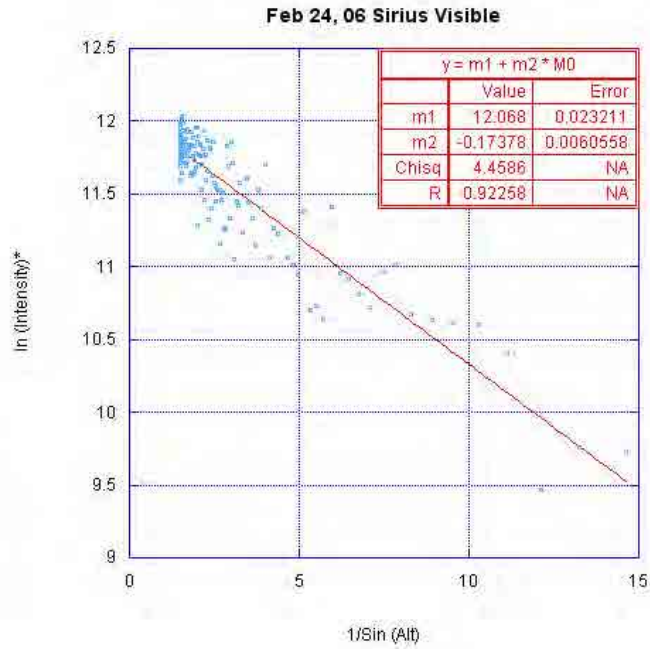

Figure 38: Feb 3, 06 IR Pyrometer
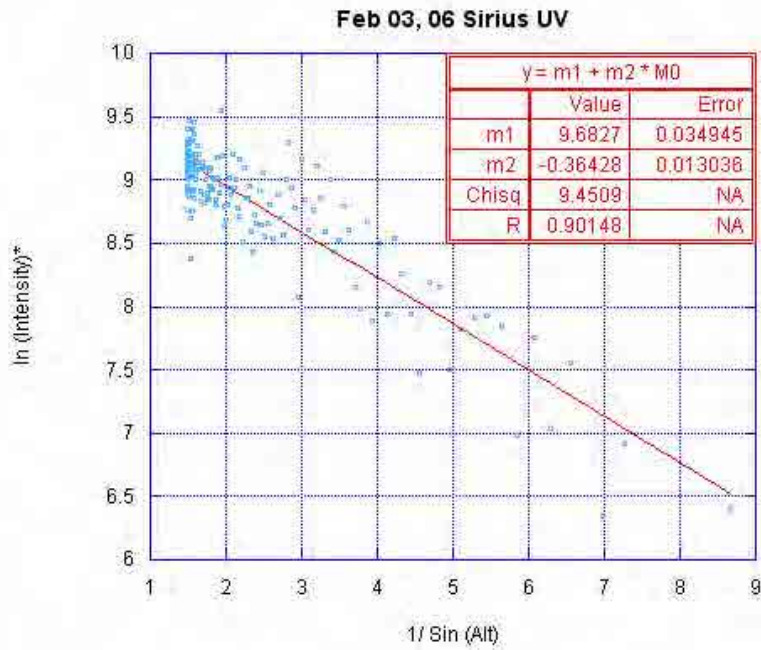
Figure 39: Feb 3, 06 UV Filter
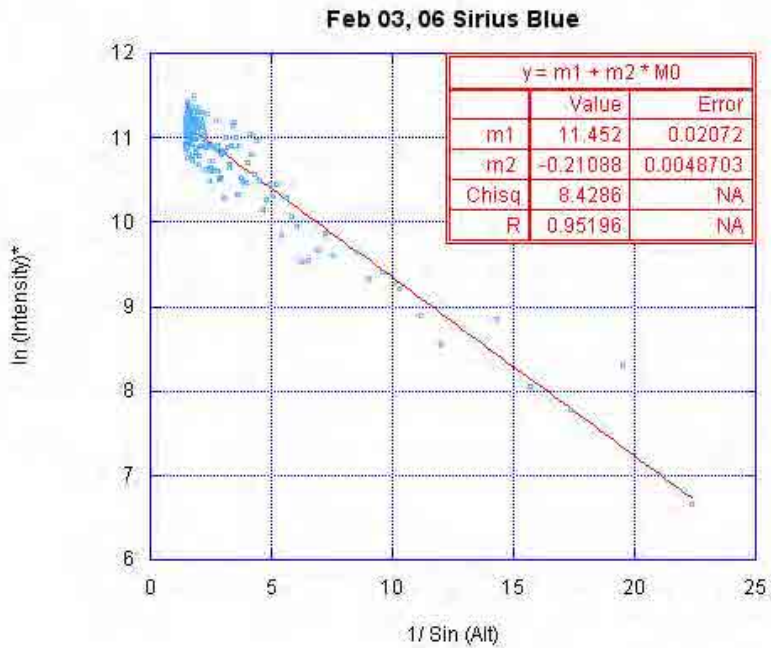
Figure 40: Feb 3, 06 Blue Filter

d

Feb 03, 06 Sirius Visible

y = m1 + m2 * M0	Value	Error
m1	11.128	0.023203
m2	-0.076907	0.0027956
Chisq	16.976	NA
R	0.88936	NA

Ln (Intensity)*

1/ Sin (Alt)
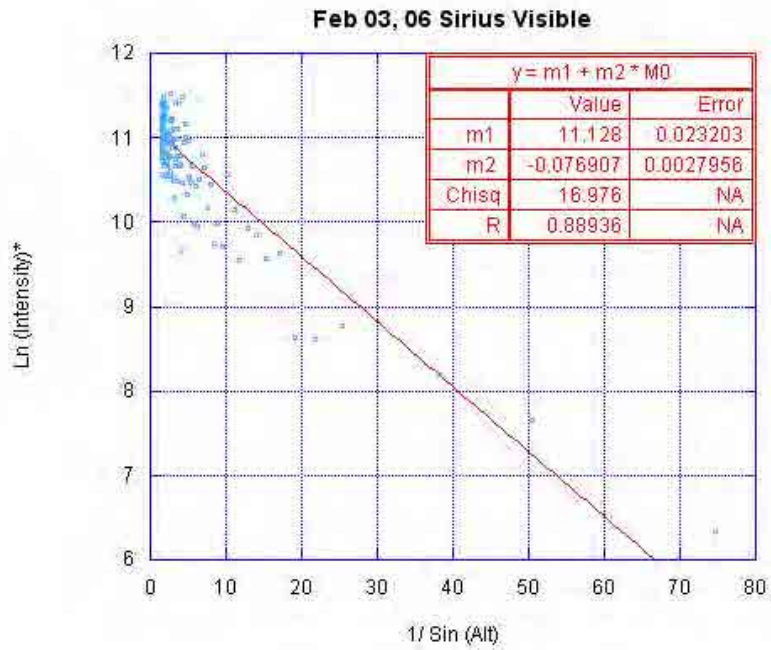
Figure 41: Feb 3, 06 Visible Filter

Feb 03, 06 Sirius Red

y = m1 + m2 * M0	Value	Error
m1	11.191	0.021294
m2	-0.05185	0.0026466
Chisq	13.871	NA
R	0.81151	NA

ln (Intensity)*

1/ Sin (Alt)
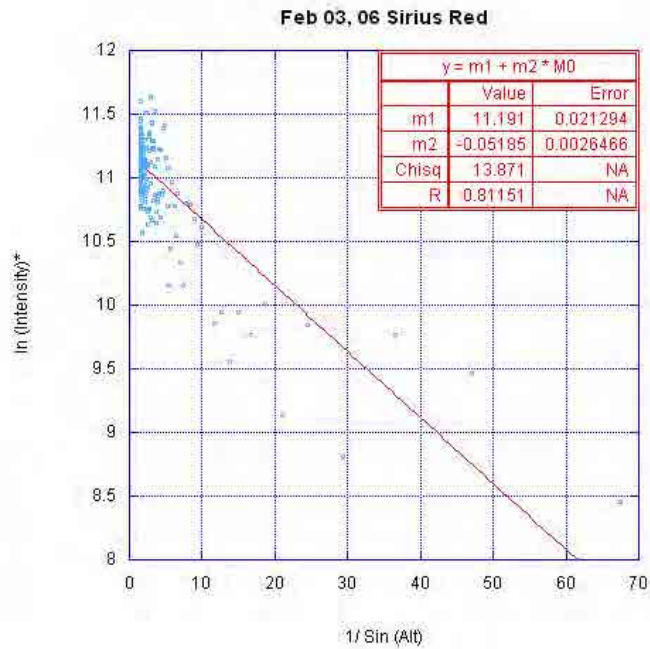
Figure 42: Feb 3, 06 Red Filter

e

Figure 43: Feb 3, 06 IR Filter

Appendix III.   February 24th 2006 Graphs

Data related to Figure 44, Figure 45, Figure 46, Figure 47, Figure 48, and Figure 49 is available at http://www.physics.utah.edu/~kwaller/Atmosphere/ .
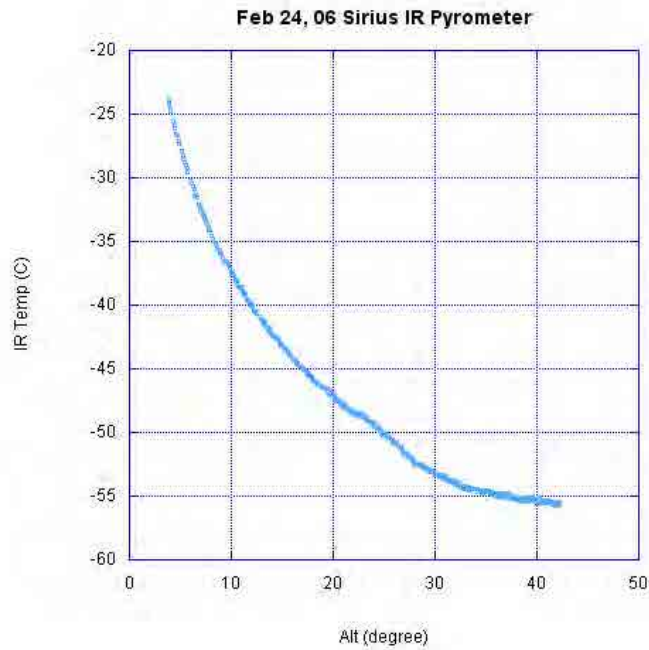
Figure 44: Feb 24, 06 IR Pyromete

Figure 45: Feb 24, 06 UV Filter

Figure 46: Feb 24, 06 Blue Filter

Figure 47: Feb 24, 06 Visible Filter
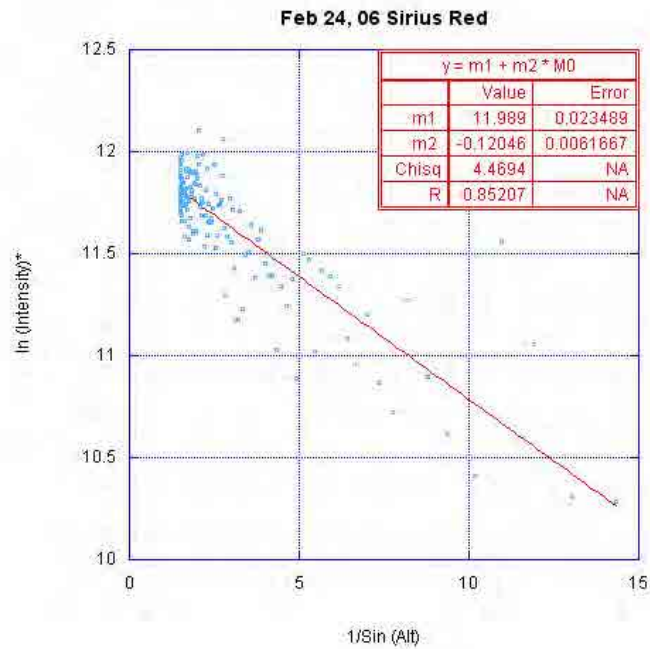
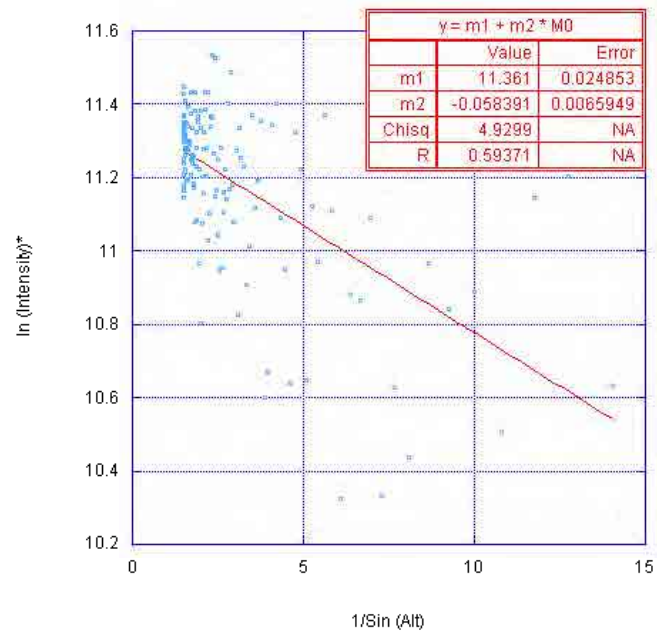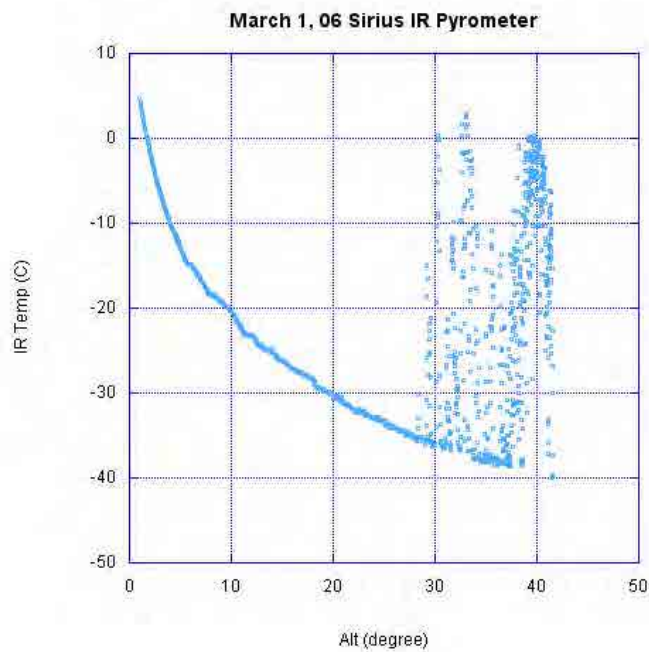
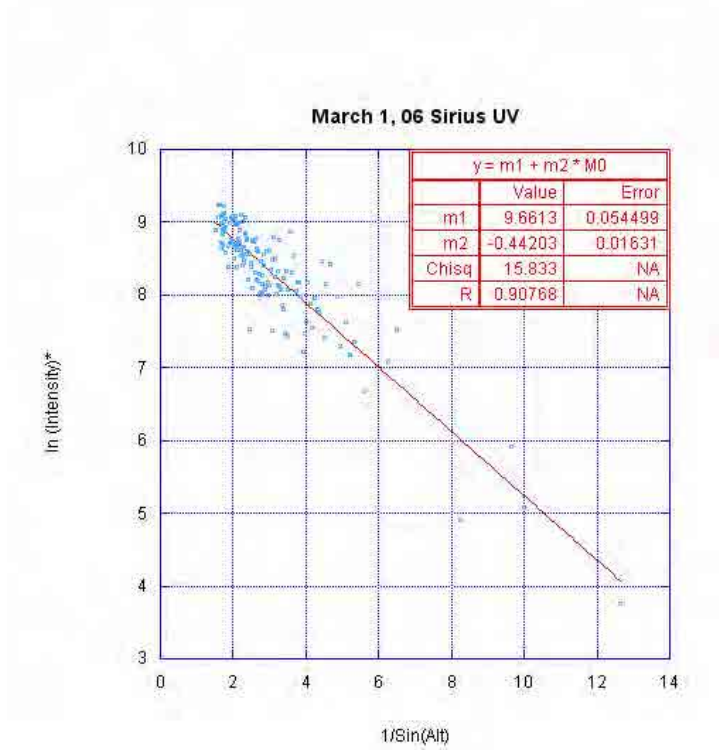**Figure 48: Feb 24, 06 Red Filter**

Feb 24, 06 Sirius IR

y = m1 + m2 * M0	Value	Error
m1	11.361	0.024853
m2	-0.058391	0.0065949
Chisq	4.9299	NA
R	0.59371	NA

ln (Intensity)*

1/Sin (Alt)

Figure 49: Feb 24, 06 IR Filter

Appendix IV. March 1st 2006 Graphs

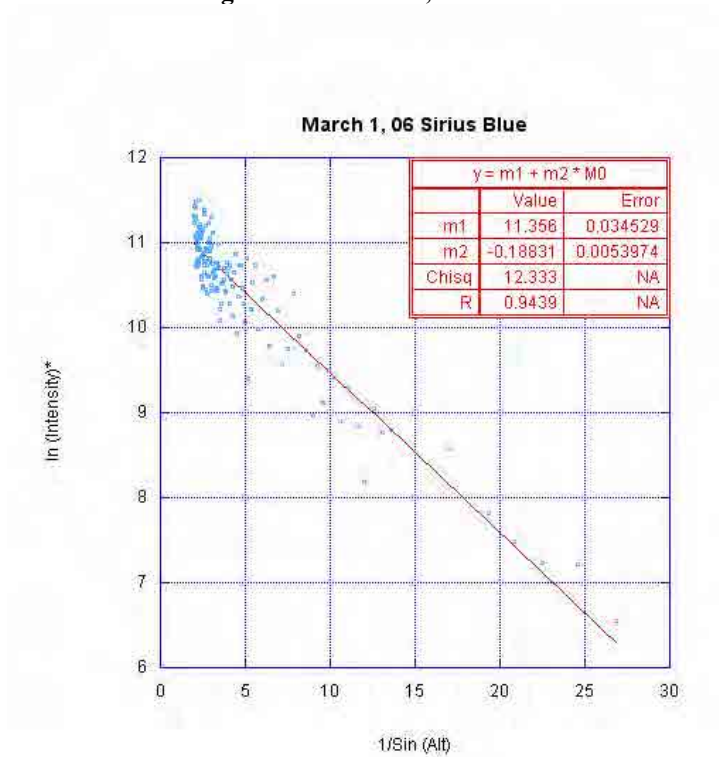Data related to Figure 50, Figure 51, Figure 52, Figure 54, and Figure 55 is available at
http://www.physics.utah.edu/~kwaller/Atmosphere/ .

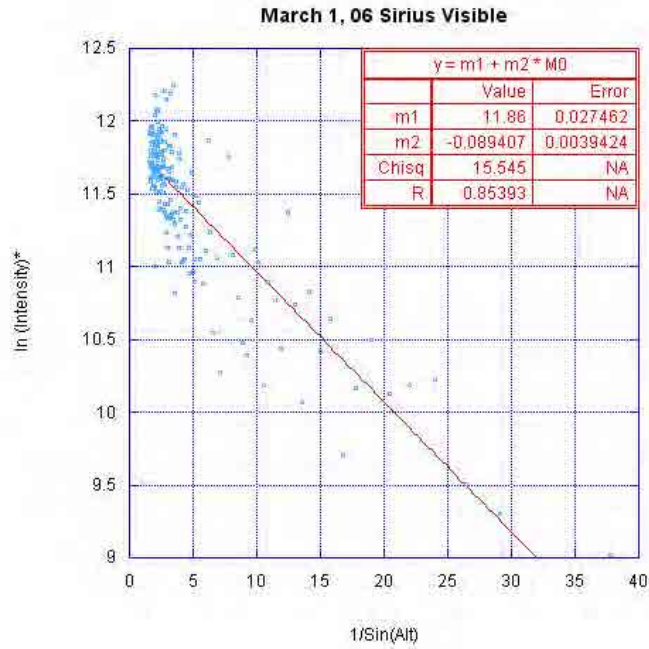**Figure 50: March 1, 06 IR Pyrometer**

Data points in Figure 50 that do not fit the atmospheric attenuation curve where omitted in the
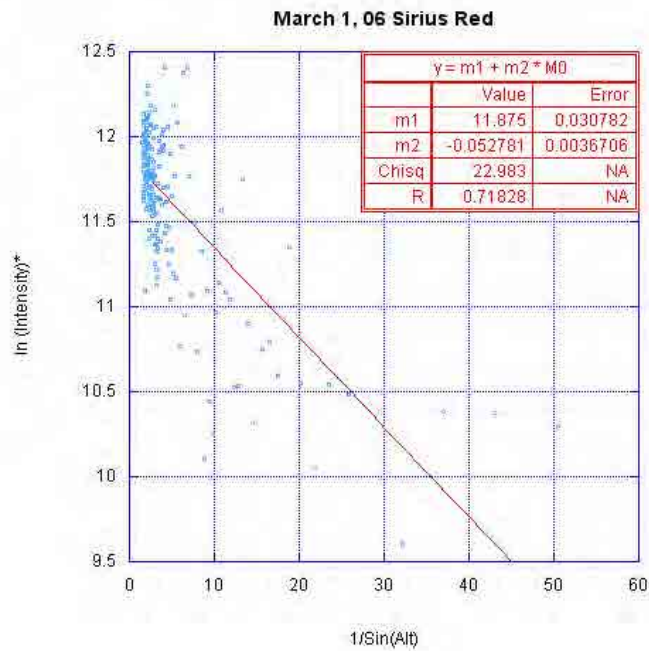following graphs.

Figure 51: March 1, 06 UV Filter

Figure 52: March 1, 06 Blue Filter

March 1, 06 Sirius Visible

y = m1 + m2 * M0		
	Value	Error
m1	11.86	0.027462
m2	-0.089407	0.0039424
Chisq	15.545	NA
R	0.85393	NA

Figure 53: March 1, 06 Visible Filter

March 1, 06 Sirius Red

y = m1 + m2 * M0		
	Value	Error
m1	11.875	0.030782
m2	-0.052781	0.0036706
Chisq	22.983	NA
R	0.71828	NA

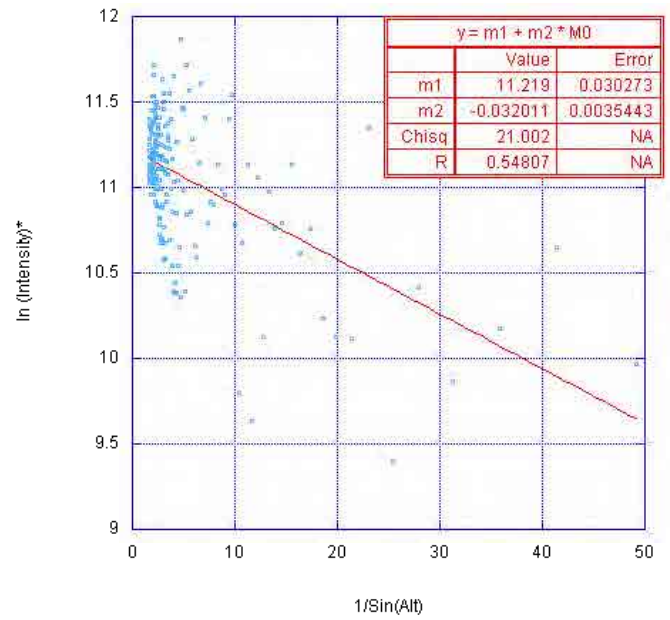**Figure 54: March 1, 06 Red Filter**

m

Figure 55: March 1, 06 IR Filter

Appendix V.   Clouds versus Star Intensity with Ultraviolet Filter

The IR pyrometer was used to detect clouds while collecting data for atmospheric attenuation. The stability of the IR pyrometer was used to choose which atmospheric attenuation data to be used for analysis.

By showing high correlation between the IR pyrometer and star intensity, it is justified to use the IR pyrometer stability to choose atmospheric attenuation data.

Data collected March 5th was used to correlate star intensity in ultraviolet to the –IR pyrometer temperature. If the star intensity in ultraviolet is correlated to the IR pyrometer, it can be assumed the star intensity for all the filters is correlated to the IR pyrometer.

The IR pyrometer was set to a 1 second response time and emissivity of 1.000. The star intensity was measured while tracking Sirius. The star intensity is measured with the CCD camera set to an exposure time of 0.12 seconds. The CCD was temperature regulated at a setpoint of 1500 for both the exposures and dark frames. A 40 X 40 pixel ROI, with background subtracted, was selected around the star and the intensity of the star was defined as,

Star Intensity = Σ Pixels above 1 Standard Deviation of the ROI Mean.

Figure 56 shows –IR pyrometer temperature and star intensity versus altitude. Pearson's *R* is shown in Figure 57.

Data related to Figure 56 and Figure 57 is available at
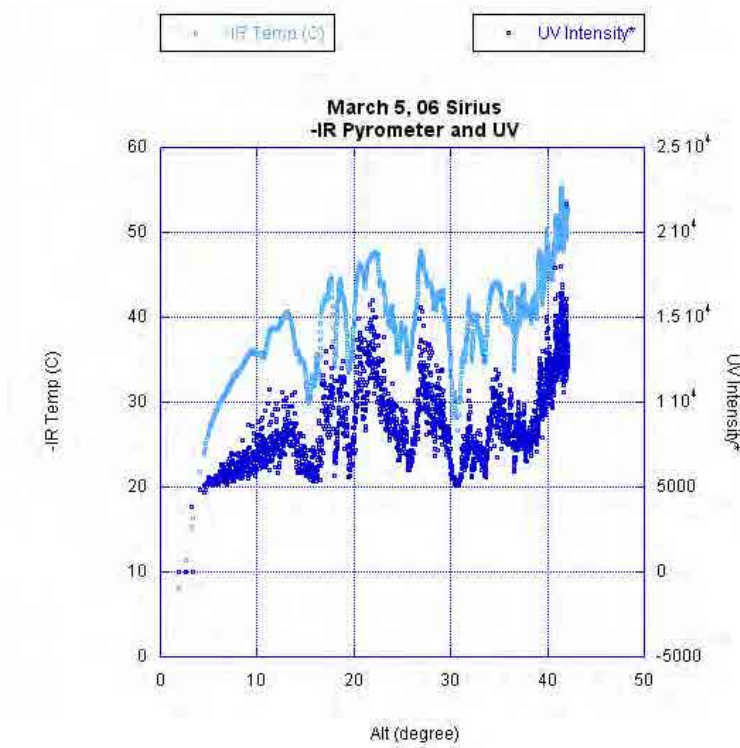http://www.physics.utah.edu/~kwaller/Atmosphere/3_05_06_Sirius_UV/Data.TXT .

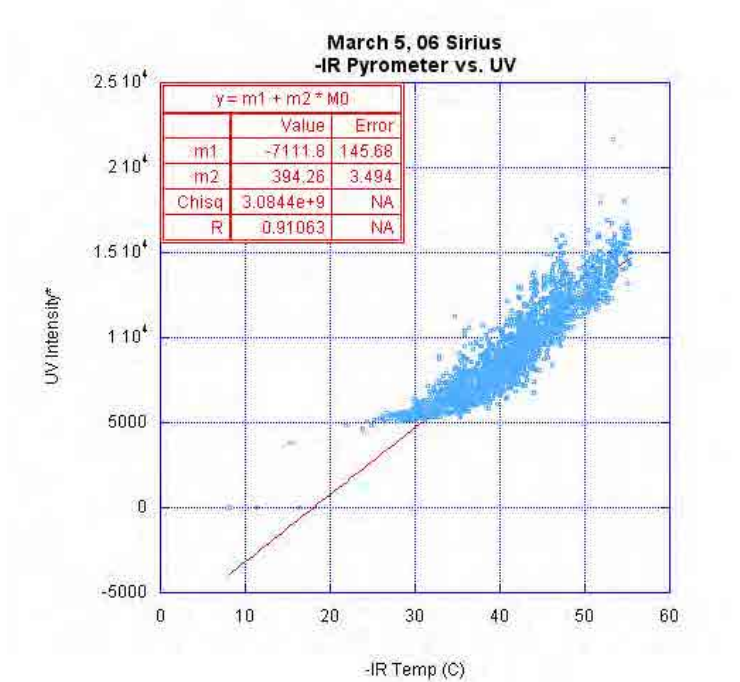**Figure 56: Ultraviolet Star Intensity and IR Pyrometer vs. Altitude**

Figure 57: Pearson's *R* for Ultraviolet Star Intensity vs. -IR Temperature

The correlation between the IR pyrometer and star intensity in ultraviolet is,

$$R = 0.91063.$$

$$R^2 = 0.82925.$$

Therefore, the IR pyrometer is 83% correlated to the star intensity in ultraviolet.

q

References

[i] VERITAS Homepage, (accessed May 4, 2006). http://veritas.sao.arizona.edu/

[ii] VERITAS Homepage, (accessed May 4, 2006). http://veritas.sao.arizona.edu/

[iii] *How Thick is the Earth's Atmosphere*, (accessed April 10, 2006). http://www.pdas.com/atmthick.htm

[iv] Walker, Gary. *Measurement of Atmospheric Attenuation via Star Tracking*, 27th ICRC, Hamburg Germany, 2002. (available at http://www.physics.utah.edu/~kwaller/Atmosphere)

[v] The MMTO Sky Camera, (accessed April 11, 2006). http://skycam.mmto.arizona.edu/

[vi] *Atmospheric Monitoring for the H.E.S.S. Project*, The 28th International Cosmic Ray Conference, (accessed April 11, 2006). http://www.mpi-hd.mpg.de/hfm/HESS/public/publications/icrc2003/008546-2.pdf

[vii] *Infrared Radiation Pyrometer KT15D Operating Instruction* (Provided with Device)

[viii] *KT15D Series – Technical Data*, (accessed April 11, 2006). http://www.heitronics.com/dnls/TD15DE04.PDF

[ix] Walker, Gary. *Measurement of Atmospheric Attenuation via Star Tracking*, 27th ICRC, Hamburg Germany, 2002. (Available at http://www.physics.utah.edu/~kwaller/Atmosphere)

[x] SBIGUDRV.DLL Version 4.44 Build 5, Santa Barbara Instrument Group.

[xi] *SBIG Universal Driver/Library Version 4.43*, Santa Barbara Instrument Group, January 2005.

[xii] *Using External Code in Labview,* National Instruments, April 2003, (accessed April 11, 2006). http://www.ni.com/pdf/manuals/370109b.pdf

[xiii] *SGIBUDRV.H Version 4.43*, Santa Barbara Instrument Group, January 2005. (Provides Definitions of Enumerated Constants in sbigudrv.dll)

[xiv] *Why Do My Clusters in LabVIEW Not Line Up With My Structures in Visual C++ - Pragma Packing with LabVIEW?* National Instruments, (accessed April 11, 2006), http://digital.ni.com/public.nsf/allkb/F7E5C9169D09E98586256AF300717B33

[xv] CFW-8A Color Filter Wheel Manual, Santa Barbara Instrument Group, 2002, (accessed April 12, 2006). http://www.sbig.com/pdffiles/cfw8man_2002b.pdf

xvi Pasken, Bob *ConnectingAutostar2Comp,* Feb. 02, 2003, (accessed April 12, 2006).
http://www.weasner.com/etx/fun/etx_star_party_2002/etx90ec-talk.zip

xvii *Meade Telescope Serial Command Protocol,* Revision L, Oct. 9, 2002, (accessed April 12, 2006).
http://www.meade.com/support/LX200CommandSet.pdf

xviii *Instruction Manual, 8″ LX90 Schmidt-Cassegrain Telescope with Autostar Hand Controller*,
Meade Instruments Corporation, 2000, (accessed April 12, 2006).
http://www.meade.com/manuals/TelescopeManuals/LXseries/LX-90_manual.pdf

xix *Correlation*, Wikipedia, April 2006, (accessed April 19, 2006).
http://en.wikipedia.org/wiki/Correlation

xx Walker, Gary. *Measurement of Atmospheric Attenuation via Star Tracking*, 27th ICRC, Hamburg
Germany, 2002. (Available at http://www.physics.utah.edu/~kwaller/Atmosphere)

xxi *Electro-Optics Handbook*, Burle Industries, Inc., Lancaster, 1974, pg 85, Fig. 7-3.

xxii *Electro-Optics Handbook*, Burle Industries, Inc., Lancaster, 1974, pg 85, Fig. 7-3.